7-5-2018

# Design and Performance Estimation of a Low-Reynolds Number Unmanned Aircraft System

Sean Lauderdale King
*Louisiana State University and Agricultural and Mechanical College*

# DESIGN AND PERFORMANCE ESTIMATION OF A LOW REYNOLDS NUMBER UNMANNED AIRCRAFT SYSTEM

A Thesis

Submitted to the Graduate Faculty of the
Louisiana State University and
Agricultural and Mechanical College
in partial fulfillment of the
requirements for the degree of
Master of Science

in

The Department of Mechanical Engineering

by
Sean Lauderdale King
B.S.M.E., Louisiana State University, 2014
August 2018

## Table of Contents

List of Tables ..... iv

List of Figures ..... v

Abstract ..... v

Chapter 1. Introduction and Design Process ..... 1
1.1 Purpose of the Design ..... 1
1.2 Design Considerations (Mission Parameters) ..... 2
1.3 Design Process and Thesis Structure ..... 5

Chapter 2. Conceptual Design Phase ..... 9
2.1 Design Equations ..... 9
2.2 Preliminary Airfoil Selection ..... 14
2.3 Analytical Solution to Finite Wing Properties ..... 18
2.4 Initial Plane Design ..... 22

Chapter 3. Preliminary Design Calculations ..... 23
3.1 Flight Mechanics and Aerodynamic Analysis ..... 23
3.2 Structural Analysis ..... 37
3.3 Powerplant Selection ..... 45
3.4 Interim Design Overview ..... 48

Chapter 4. Detail Design Calculations ..... 49
4.1 Fault Tree ..... 49
4.2 Final Design Weight Buildup ..... 50
4.3 Detailed Flight Mechanics ..... 51
4.4 Detailed Structural Analysis ..... 54
4.5 Final Design Overview ..... 59

Chapter 5. Final Iteration Performance Estimation ..... 61
5.1 Takeoff ..... 61
5.2 Climb ..... 62
5.3 Level Flight ..... 64
5.3.2 Endurance and Range ..... 66
5.4 Landing ..... 75
5.5 Performance Review ..... 76

Chapter 6. Conclusion ..... 77

References ..... 79

Appendix A. Market Survey and Differentiation ..... 81
A.1 Review of Market Competition ..... 81
A.2 Potential Design Modules ..... 82
A.3 Manufacturing Cost Estimate ..... 83

Appendix B. FAA FAR Part §23 Design ..... 85
B.1 Maneuvering Loading ..... 85
B.2 Gust Loading ..... 85
B.3 Landing Loading ..... 86

Appendix C. Dynamic Thrust Estimation ..... 87
C.1 Theory ..... 87
C.2 Code Validation ..... 88
C.3 Results ..... 89

Vita ..... 92

# List of Tables

Table 1. Qualitative summary of FAA Part 23 design criteria ..... 3

Table 2. Qualitative and quantitative design specifications ..... 7

Table 3. Summary table of 2D airfoil lift characteristics ..... 17

Table 4. Drag minimization constraints on optimization space ..... 25

Table 5. Delta derivative validation table ..... 32

Table 6. Stress summary table ..... 43

Table 7. Design weight buildup ..... 50

Table 8. Eigenvalues of dynamic stability modes ..... 54

Table 9. Landing load maximum principal stress convergence table ..... 56

Table 10. Maneuvering loading maximum principal stress convergence table ..... 57

Table 11. Full fuel underdamped dynamic stability responses ..... 68

Table 12. No fuel underdamped dynamic stability responses ..... 68

Table 13. Design parameters met and summary of the vehicle parameters ..... 78

Table 14. Table of market competitors ..... 82

Table 15. Common market survey results for modules ..... 83

Table 16. Major subsystem cost summary ..... 83

# List of Figures

Figure 1. General plane design process ..... 6

Figure 2. General objectives of a UAS ..... 8

Figure 3. Basic flight forces of a tailless, pusher UAS with internal payload body ..... 11

Figure 4. Fuselage-centered coordinate force resolution diagram ..... 12

Figure 5. Simplified wing loading analysis ..... 13

Figure 6. S5020, MH 60 and MH 45 airfoil sections ..... 15

Figure 7. Lift curve comparison of MH45, MH 60, and S5020 airfoils with respect to airfoil angle of attack ..... 16

Figure 8. Drag curve comparison of MH45, MH 60, and S5020 airfoils with respect to airfoil angle of attack ..... 16

Figure 9. Moment curve comparison of MH45, MH 60, and S5020 airfoils with respect to airfoil angle of attack ..... 17

Figure 10. Built-up wing cross section for an S5020 wing ..... 21

Figure 11. Semi-monocoque wing cross-section for an S5020 and a foam-filled wing. ..... 21

Figure 12. Foam-filled wing cross section for an S5020 wing ..... 21

Figure 13. Preliminary plane design ..... 22

Figure 14. Effect of wing sweep and aspect ratio of a finite wing on theoretical Oswald efficiency ..... 25

Figure 15. Basic planform geometry of Project UAS ..... 27

Figure 16. Drag buildup of zero-lift drag and induced drag for an intermediate design iteration ..... 28

Figure 17. Swept cord of the aircraft ..... 30

Figure 18. 3D VLM lift slope curves for $\delta$= 0,1,2,3 ..... 31

Figure 19. Restoring moment for various planform configurations ..... 34

Figure 20. xflr visualization of Project UAS directional stability additions ..... 35

Figure 21. Estimated flight envelope at sea level and 10,000 ft ..... 36

Figure 22. Frame payload section with max stress component highlighted ..... 37

Figure 23. Free body diagram of fuselage frame section with full half-lift load applied ..... 38

Figure 24. Landing load locations on the payload fuselage section ..... 39

Figure 25. Lift and moment spanwise distribution for an intermediate design iteration ..... 40

Figure 26. Drag spanwise distribution for an intermediate design iteration ..... 41

Figure 27. Pure spar loading deflection curve ..... 44

Figure 28. Power required at sea level and 10,000 ft ..... 46

Figure 29. Power budget curves for all physical and legal flight regimes ..... 47

Figure 30. Simplified project vehicle fault tree ..... 49

Figure 31. Elevon deflection required for trim as a function of level flight speed ... 52

Figure 32. Root locus plot for underdamped modes ..... 53

Figure 33. Converged FEA results for landing loading on frame ..... 55

Figure 34. Wing maneuvering loading ..... 56

Figure 35. Isometric view of wing skin deflection ..... 58

Figure 36. Bottom view of wing skin deflection ..... 59

Figure 37. CG speed with respect to the distance travelled in hand-launch ..... 62

Figure 38. Wide open throttle vertical climb speed ..... 63

Figure 39. Steady, level turn bank angle ..... 64

Figure 40. Minimum turning radius of vehicle for two limiting cases ..... 65

Figure 41. Short period chord-wise velocity response ..... 70

Figure 42. Phugoid chord-wise velocity response ..... 71

Figure 43. Dutch roll span-wise velocity response ..... 72

Figure 44. Short period position estimation ..... 73

Figure 45. Phugoid mode position response ..... 74

Figure 46. Dutch roll position response ..... 75

Figure 47. Simplified views of the project UAS ..... 78

Figure 48. Power consumption and max speed of various UAS ..... 81

Figure 49. Section view of a typical propeller airfoil with force and velocity diagrams ..... 87

Figure 50. Static thrust estimation curves ..... 88

Figure 51. Dynamic thrust estimation curves ..... 89

Figure 52. 10x6-4 Propeller thrust force estimate and comparison to APC data ..... 90

Figure 53. 10x6-4 propeller normal force estimate and comparison to APC data ..... 91

# Abstract

The purpose of this thesis is to conceptually design a fixed-wing unmanned aircraft systems (UAS) with a higher flight-time and top stable speed than comparable systems. The vehicle adheres to specifications derived from the client, the market, and the Federal Aviation Administration (FAA). To broadly meet these requirements, the vehicle must fly for a minimum of three hours, return to the original flight path quickly if perturbed, and must be hand-launched. The vehicle designed must also have a large potential center of gravity movement to allow for customization of the planform and client customization.

An iterative design process was used to quickly perform tradeoff analysis and to refine the overall design. Analysis is split into two categories: flight mechanics, and structural analysis. Flight mechanics determines the flight regimes in which the vehicle is assumed to fly and the aerodynamic load factors used in structural analysis (up to 3.8 times the level flight loading. The change in lift due to skin deflection is determined to be negligible under maximum gust conditions. The vehicle itself is stable in all flight conditions, except the spiral mode; however, the addition of a stability augmentation system (SAS) can allow for corrections and autonomous flight in future iterations.

The vehicle can operate between sea-level and a maximum flight altitude of 10,400 ft as required by the FAA in 14 CFR Part 107. The final flight time of 24 hours comparable to high-end UAS sold in the U.S. Further, the vehicle is stable in speeds up to 100 mph, allowing for the maximum legal speeds of travel.

# Chapter 1. Introduction and Design Process

The unmanned aircraft system (UAS) design addressed in this thesis operates in the low Reynolds number flight regime (Re<1,500,000) – characterized by small wing cross-section, and/or low speed flight. An initial configuration was determined using basic aerodynamic relations to allow for quicker iteration of internal structures, and wing geometry. Iterations of the design were performed using standard analytical solutions to planform wing geometry, flight forces, and structural considerations from references [4], [5], and [6]. To mitigate the main failure modes identified by a fault tree analysis, closed-form solutions are refined through numerical analysis. The final design for this thesis is comparable in flight time to high-end internal combustion vehicles, with better gust and maneuvering performance while maintaining an estimated initial purchase price of $10,000.

## 1.1 Purpose of the Design

The current market of low Reynolds number unmanned aircraft systems (UAS) is focused on multi-rotor vehicles – the most common being a quadcoptor. A market exists, however, for longer flight times and more gust-stable flight. This necessitates the design of a fixed-wing craft. A market also exists for a single, modular planform that allows users to customize their experience without the undue burden of purchasing multiple UAS packages (Appendix A). The purpose, therefore, of this thesis is to design a long-endurance UAS that is stable with many

potential end-user driven payload types and configurations such as air quality sampling, 3D scanning through camera vision, or package delivery.

## 1.2 Design Considerations (Mission Parameters)

Mission parameters, or design constraints, were derived from three distinct sources: the client, the regulations of the Federal Aviation Administration (FAA) regulations (14 CFR Part 23 and 107), and potential end-users in industry. Client specifications are those required as an absolute minimum for investment. The FAA regulations provide the designer with quantitative goals to allow the vehicle to perform nominally in all reasonable U.S. flight conditions. Potential industry end-users determine the marketability of the design.

### 1.2.1 Client Specifications

The client for the Project UAS established certain criteria that must be met. The vehicle must fly for at least three hours at speeds above 25 kts to allow for less downtime in the surveying industry. Additionally, the UAV must be able to carry a useful payload of five pounds, have a pusher propeller configuration, and be capable of hand-launch. As mentioned in section 1.1, a modular design is also required by the client, meaning that a single vehicle can be used for multiple applications without the end user purchasing job-specific vehicles.

The client's criteria create several initial design considerations. To accomplish a rotational hand launch, the stall speed of the plane (the minimum physically possible flight speed) is required to be low, and the wing-span minimized to reduce the total centrifugal force on the connections while being launched. Hand-

launch is often facilitated by the addition of a high engine thrust-to-weight ratio (T/W). However, the increase in initial thrust requires an increase in fuel and a higher weight engine. A balance of these design considerations must be reached in the preliminary design phase. The flight dynamics of a UAV change significantly with the location of the center of gravity (CG), therefore, each combination of payloads, as well as a UAV without a full load, must place the CG within an acceptable range. The dynamics of the flight must also be considered with full fuel weight and with no fuel to ensure that a gust will not cause significant camera distortion for any potential 3D point cloud data.

### 1.2.2 FAA Regulations

The FAA has established regulations for small aircraft at 14 Code of Federal Regulations (CFR) Part 23. Adherence to these regulations impose additional quantitative specifications for the design. Examples include structural load factors, performance, and stability criteria. These criteria will be used in the conceptual and detailed design phases to ensure that the final vehicle is airworthy. Relevant CFR sections will be quantified and referenced as justification for design decision in Chapters 2 to 4. Relevant design criteria are summarized in Table 1.

Table 1. Qualitative summary of FAA Part 23 design criteria

| Criteria | Sections | Summary |
|---|---|---|
| Aerodynamic | 23.21 – 23.161, 23.231 – 23.253 | The plane must have sufficient performance analysis to predict all reasonable flight loads and stability conditions. |
| Stability | 23.171 – 23.221 | The plane must remain directionally stable under all expected flight loads. |
| Structural | 23.301 – 23.575 | The plane must withstand all expected loads within a specified flight envelope. |

Design of the powerplant itself is not a consideration of the Project UAS. The powerplant analysis in later chapters serves to minimize the total combined powerplant and fuel weight. This is performed in the preliminary and conceptual design phases in Chapter 2 and 3.

### 1.2.3 Market-Derived Specifications

Specifications for the design are also derived from market values and considerations of the end user. The market value for the planform must be under $10,000 to allow small businesses and contractors to purchase the Project UAS. The base price was determined through a market survey of potential customers: small businesses, contractors, and high-dollar value hobbyists, and a review of manufacturers' specifications (Appendix A). The UAS market in the Gulf South region of the U.S. focuses mainly on surveying, air quality sampling, and package delivery. Modules, or UAS internals, can be designed to meet each of these regional markets. However, the module designs themselves are not addressed in this thesis. The planform, though, can accommodate a variety of modules by having a uniform inner-body diameter, and a large range of CG travel.

The flight mechanics and performance of the plane are also influenced by the market. The headwind range of the plane must exceed 200 miles to perform successful delivery to offshore rigs (Appendix A). The number one response from the market survey was imaging capability. For the vehicle to map large areas even in non-optimum conditions, and reduce downtime for surveying, both the distance

travelled and change in total speed must be small in response to a gust. Therefore, vehicle dynamic stability in the longitudinal plane must be either overdamped or allow for negligible deviations in flight path.

The majority of designs available on the market are either unable to carry the client-stated goal of 5 lb, are cost prohibitive to a general consumer, or are not modular in design. As such, the current market has few designs to perform multiple tasks that a small-to-midsize company can afford. Additionally, the constraint that the plane is hand-launched is not met by the planes having useful payloads in excess of 5 lb.

### 1.3 Design Process and Thesis Structure

The following section outlines the process followed in designing a low Reynolds number UAS. The general process is iterative and entails three design phases: conceptual design, preliminary design, and detail design [4]. The chapters in this thesis follow this structure as well. Chapter 2 entails the conceptual design of the vehicle, Chapter 3 includes the analytical solutions and results from the preliminary design phase, and Chapter 4 contains the numerical analysis for weight reduction of the vehicle. Detailed calculations of the vehicle performance are not a part of this design process, but can be found in Chapter 5. Figure 1 broadly outlines the types of analysis performed in the design process. The testing phase of the general design process is not addressed in this thesis; however, the conceptual design in this thesis can be fabricated and tested if desired.

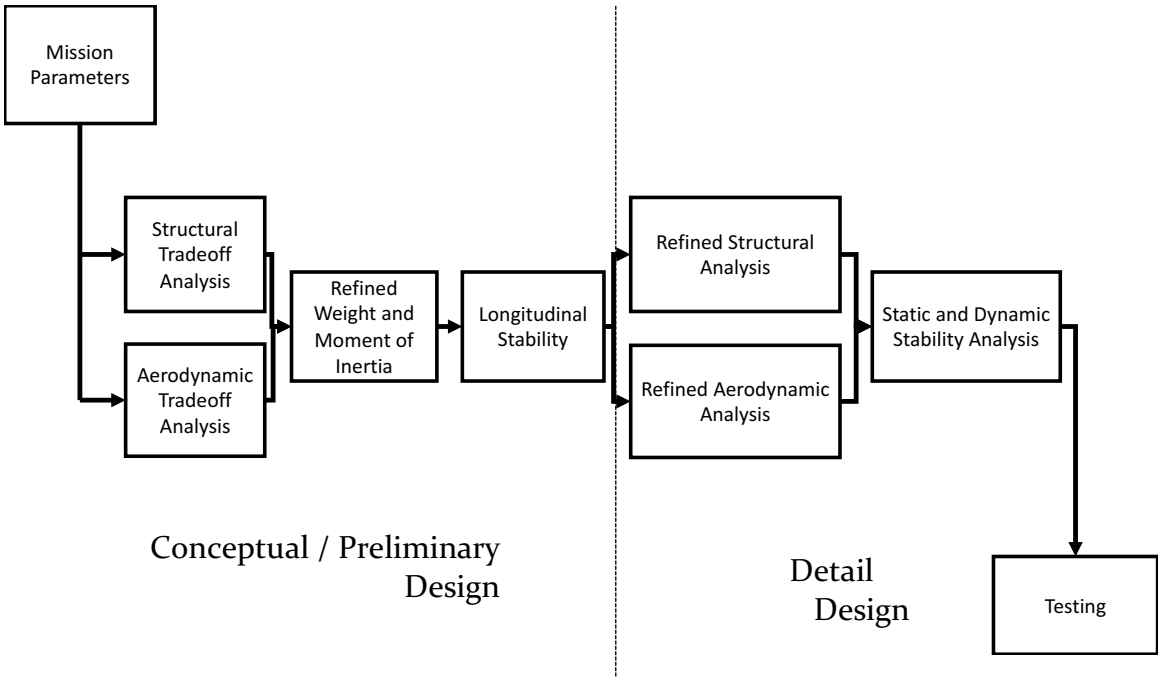


Figure 1. General plane design process

The conceptual design process entails analytical sizing of all relevant UAV subsystems, for example the wings, fuselage, and powerplant. The conceptual design phase is characterized by determining the mission parameters and ideation of multiple planforms that satisfy mission parameters. Tradeoff analysis is used in this phase to inform the designer as to which solutions are feasible to analyze in the preliminary design process. More detailed analytical solutions are then used in preliminary design to ensure statically stable flight, structural integrity, and reduce total planform cost and weight. The detail design phase refines the design to further reduce the total vehicle weight and mitigate any potential failure modes identified in fault tree analysis. The detail design section also focuses on reducing the total operational cost of the vehicle though endurance and range calculations and minimization of plane trim drag. Preliminary design analysis is refined in this phase

using numerical methods such as finite element analysis (FEA) and computational fluid dynamics (CFD). The initial mission parameters that drive all analysis in Chapters 2 through 4 are summarized in Table 2.

Table 2. Qualitative and quantitative design specifications

| **Client Driven** | **FAA Driven** | **Market Driven** |
|---|---|---|
| Fly for 3+ hours | Load Factor of 3.8 | Little user input |
| 5 lb payload | Factor of Safety 1.5 | 3+ payload modules |
| High T/W | 14% CG travel | 200 mile range |
| Cruise > 25 kts | | |
| Stall Speed < 20 ft/s | | |
| Tailless vehicle | | |
| 72 in wing span | | |

### 1.3.1 Design Objective Summary

Using the specifications listed in Table 2, and combining the qualitative constraints given in Appendix A, an objective tree can be developed. The broad objectives of any UAS are to take off, maintain level flight, and land. A more detailed visual representation of how these goals can be broadly met is given in Figure 2. The figure is, by nature, non-solution specific, so many of the specifications seen in Table 2 are not listed.

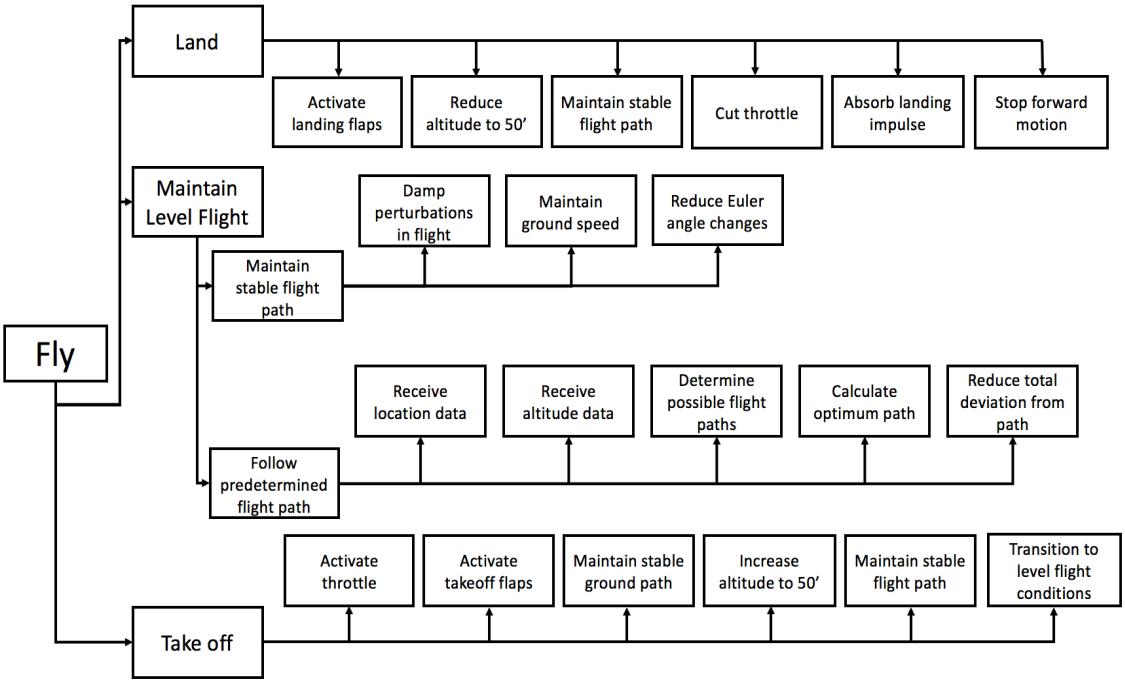


Figure 2. General objectives of a UAS

Throughout the remainder of the thesis, objectives in Figure 2 will be referenced when each sub-function is met in either design or in the following performance analysis section.

# Chapter 2. Conceptual Design Phase

The conceptual design phase entailed in this chapter uses general plane design guides from references [5] and [6], as well as back-of-the-envelope flight force estimations to determine a planform that meets the basic constraints and allows for iteration on feasible design ideas. The main types of equations used, some preliminary results, and a first iteration overview are discussed in this chapter. Chapter 3 refines this analysis using analytical methods to reduce the total vehicle weight, quantify flight forces, and to ensure stable flight.

## 2.1 Design Equations

The main tradeoff analysis used to improve design iterations includes flight mechanics and general planform structural integrity. The main equations for design are the balance of forces and moments in three directions, and the ability of the planform to maintain structural integrity in limit loads as per 14 CFR Part §23.303.

### 2.1.1 Design Variables

The key variables used for design in this thesis are listed below with their corresponding definition.

| | |
|---|---|
| L ..... Lift Force | β ..... Sideslip Angle |
| D..... Drag Force | γ ..... Bank Angle |
| B ..... Wing Side Force | $P_R$..... Power Required |
| a.....Lift Curve Slope | $P_A$ ..... Power Available |
| m..... Moment Curve Slope | $V_S$ ..... Stall Speed |
| M..... Pitching Moment | $V_C$ ..... Cruise Speed |
| l..... Rolling Moment | $V_D$ ..... Dive Speed |
| n..... Yawing Moment | $V_G$ ..... Gust Speed |
| *N*..... Wing Normal Force | n ..... Maneuvering Load Factor |
| *A*..... Wing Axial Force | $n_g$ ..... Gust Load Factor |
| $C_L$..... Lift Coefficient | t/c.....Thickness Ratio |
| $C_D$..... Total Drag Coefficient | A ..... Aspect Ratio |
| $C_{Do}$..... Zero-Lift Drag Coefficient | b ..... Wing Span |
| $C_M$..... Moment Coefficient | c ..... Chord Length |
| α ..... Angle of Attack | $\bar{c}$ ..... Mean Aerodynamic Chord |

The variables listed in this section are commonly used throughout the plane design process. Less common variables will be defined at the appropriate locations within this thesis.

### 2.1.2 Flight Mechanics Overview

The forces acting on a simple, tailless UAV are highlighted in Figure 3.

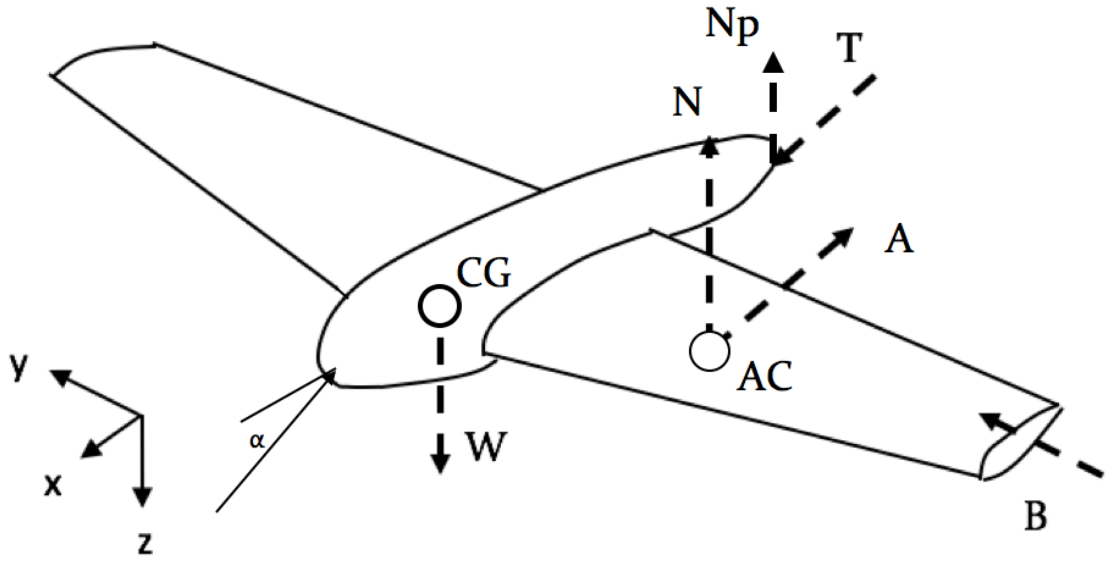


Figure 3. Basic flight forces of a tailless, pusher UAS with internal payload body

Because the motion of an aircraft is mostly in the x-z plane (pitch plane), a simplified model can be used at the outset that assumes only one angle, the angle of attack (α), which is the angle between the freestream and the flight path of the plane. A potential wing incidence angle ($i$), or the inherent geometric angle of attack of the wing, can also be combined with the total angle of attack for force resolution. Shown in Figure 3 are the body-centered forces on the UAV. This is a correction from wind-centered coordinates (dashed lines in Figure 4) to body-centered coordinates (solid lines) and are defined as

$$N = \mathrm{L}\cos\alpha + \mathrm{D}\sin\alpha \tag{1.1}$$

$$A = \mathrm{D}\cos\alpha - \mathrm{L}\sin\alpha \tag{1.2}$$

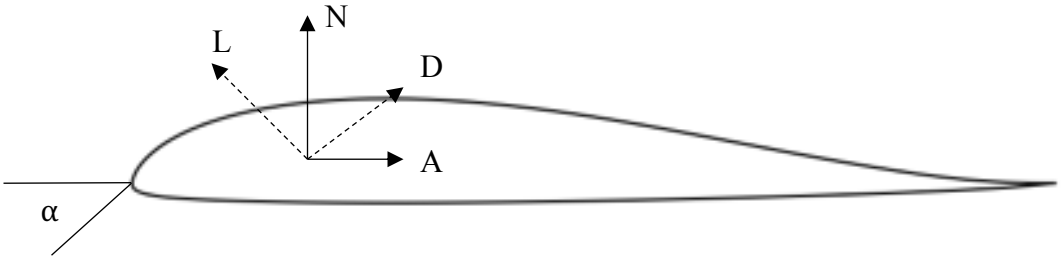

Figure 4. Fuselage-centered coordinate force resolution diagram

Here, N is the plane combined normal force, and A is the plane combined axial force. The sum of forces in each direction can be easily shown to be

$$\Sigma F_z = L\cos\alpha + D\sin\alpha - W \quad (2.1)$$

$$\Sigma F_x = D\cos\alpha - L\sin\alpha - T \quad (2.2)$$

$$\Sigma F_y = B \quad (2.3)$$

For all reasonable flight conditions in which the UAV is expected to operate, as per FAA FAR Part 23, balance of the above forces must be achieved. A reduction in the use of control surfaces to maintain the path increases the flight time of the plane by reducing trim drag and increasing total UAV endurance. The loading on the plane is also a function of these flight forces, and reduction of the forces can also reduce the total weight of the plane.

### 2.1.3 Structural Analysis Overview

Structural analysis throughout this thesis uses flight forces and assumptions summarized in Figure 5, where the wing is modelled as a cantilever beam fixed at the root, and the lift loading is elliptical.

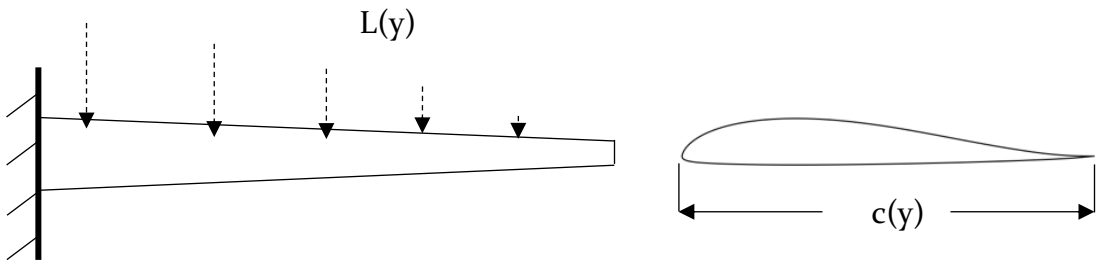


Figure 5. Simplified wing loading analysis

With the assumption that a wing can be modelled as a cantilever beam with only lift loading the analysis is reduced to the integral equation

$$\frac{\sigma_{ut}}{n_{max}} = \int_0^{b/2} \frac{L(y)(t/c)c(y)}{I(y)} dy \qquad (3)$$

where L(y) is the span-wise lift loading function, $(t/c)$ is the airfoil thickness ratio, c(y) is the chord function, and I(y) is the second moment of area distribution along the wing. From the ultimate strength ($\sigma_{ut}$) of the wing components, and the estimations of lift loading from either analytical or numerical methods, the required second moment of area can be determined. The limit loads ($n_{max}$) on the design are found at 14 CFR Part §23.333-337. The plane is, in maneuvering and gust loading, designed to withstand the limit loads, and ultimate loading ($1.5n_{max}$), adherent to 14 CFR Part §23.303. The calculated load factors required by the FAA can be found in Appendix B.

### 2.1.4 Numerical Analysis Tools

To quickly analyze the 2D characteristics of an aifoil, xflr v6.32 is used. This software is a graphic user interface that combines xfoil and Athena Vortex Lattice (AVL) software. The 2D characteristics are found using inviscid flow superposition and coupling the solver with viscous momentum conservation equations to estimate

the performance of an infinite wing [18]. The primary finite element analysis (FEA) software used is ANSYS Mechanical APDL 17.0. All numerical analysis is compared first to theory to determine the validity of the solution and then the numerical uncertainty is estimated using a method proposed in Reference [3].

## 2.2 Preliminary Airfoil Selection

The airfoil cross-section determines the lift and moment characteristics of the plane. These characteristics determine the flightworthiness of the plane through the system of equations in Equations 2.1 – 2.2. There is no pitch stabilizing moment created by a traditional vehicle empennage and elevator in a tailless UAS. Therefore, all airfoils considered were self-stable, or reflexed airfoils to reduce the total pitching moment on the vehicle. Rather than extensive wing twist, or a lower lift symmetric airfoil, a self-stable airfoil allows for ease of manufacturing and proper longitudinal performance [5]. Each airfoil section considered, a Selig 5020, and two Martin-Hepperle airfoils (60 and 45), can be seen in Figure 6. These airfoils were considered due to their low moment coefficients, and their high maximum lift coefficient when compared to other self-stable airfoils.

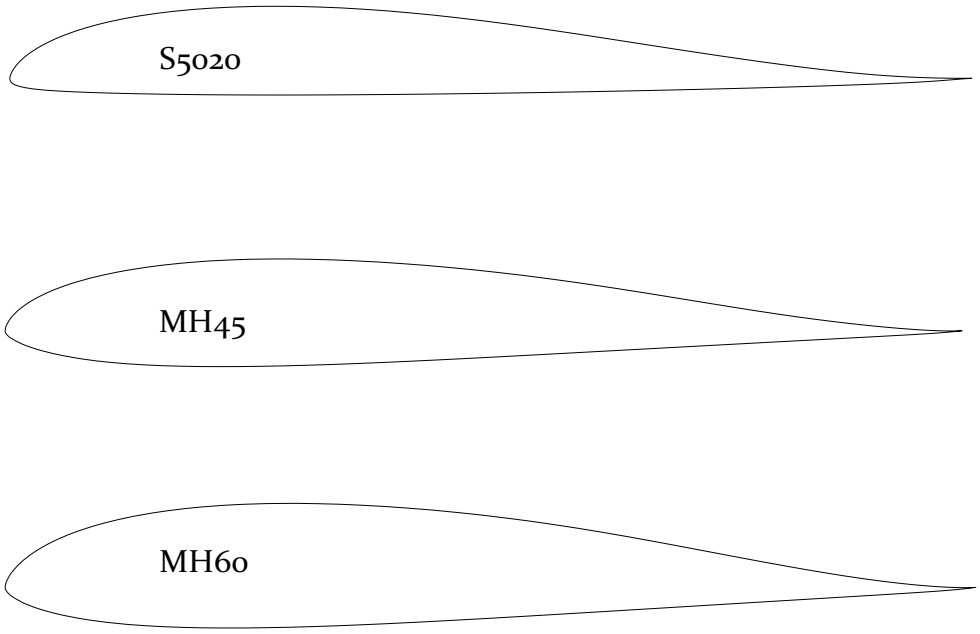


Figure 6. S5020, MH 60 and MH 45 airfoil sections

Comparison lift curves, drag curves, and moment curves of three converged two-dimensional airfoils at Re 500,000 can be seen in Figures 7 through 9.

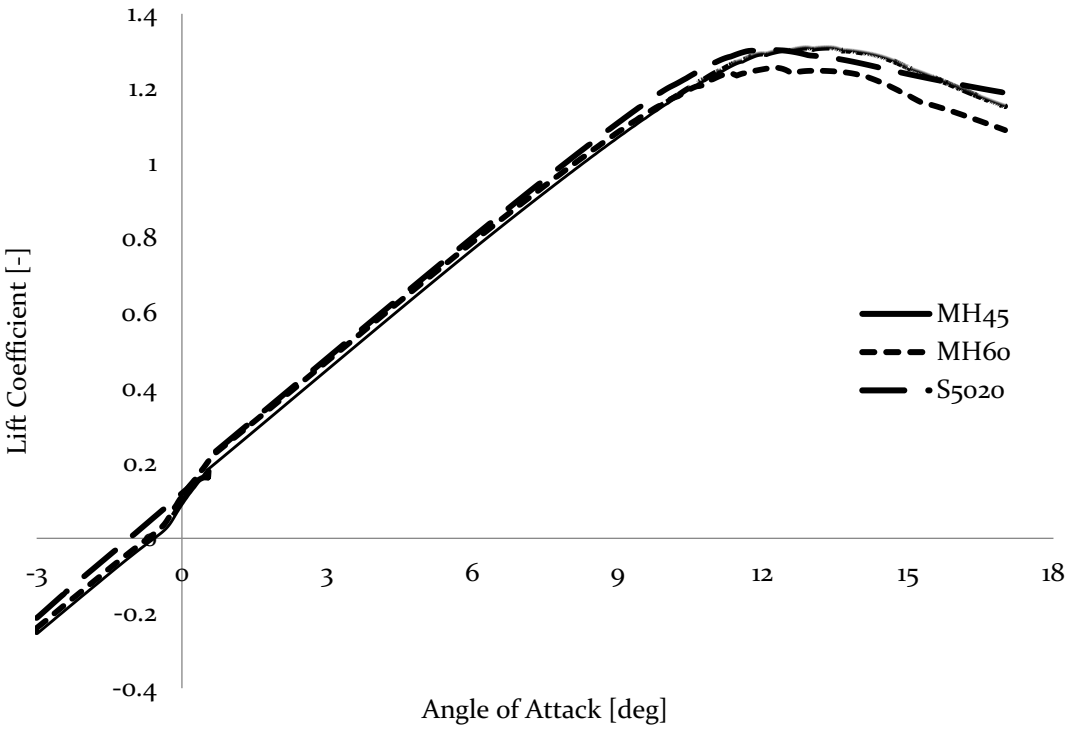


Figure 7. Lift curve comparison of MH45, MH 60, and S5020 airfoils with respect to airfoil angle of attack

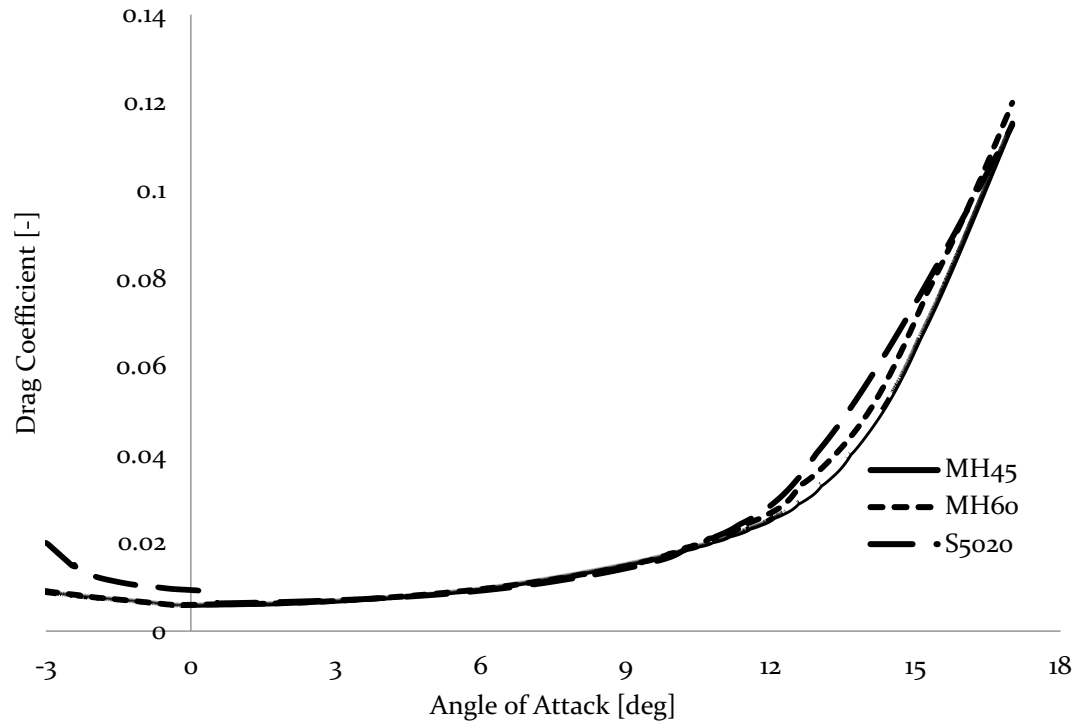


Figure 8. Drag curve comparison of MH45, MH 60, and S5020 airfoils with respect to airfoil angle of attack

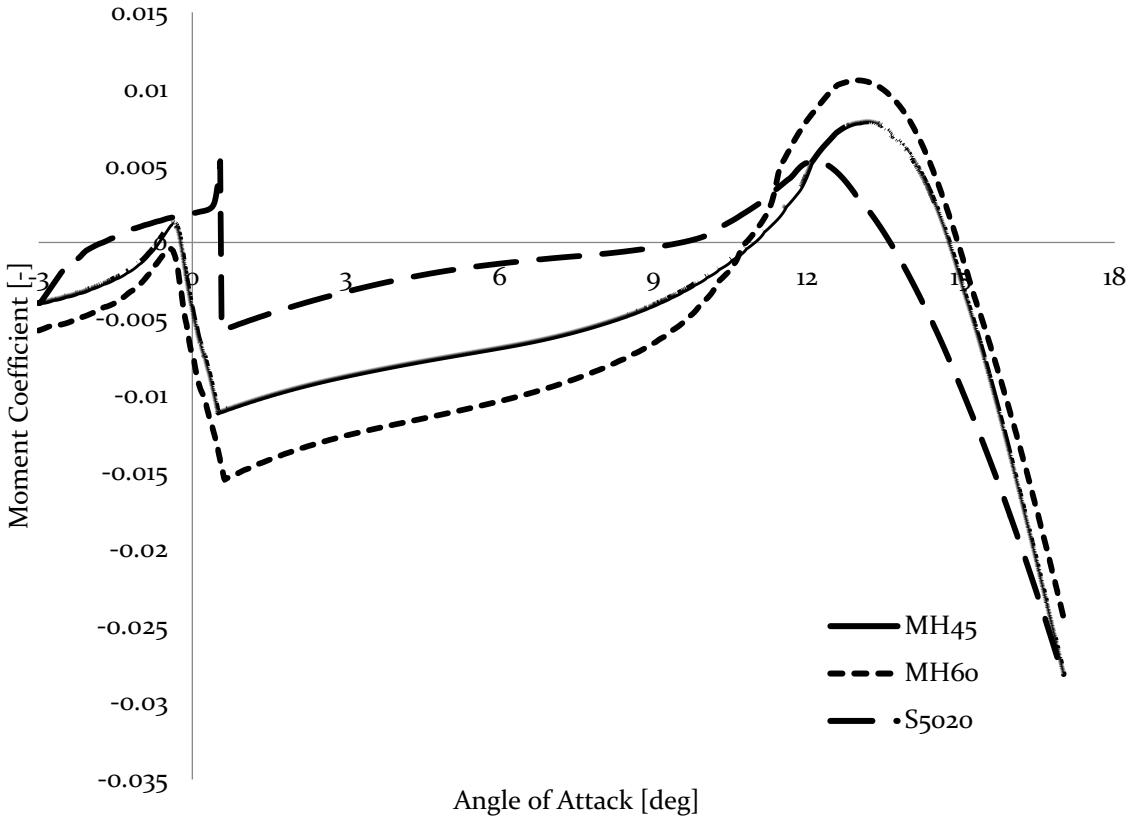


Figure 9. Moment curve comparison of MH45, MH 60, and S5020 airfoils with respect to airfoil angle of attack

The difference between the 2D lift characteristics of the airfoils is minimal; and key features are summarized in Table 3.

Table 3. Summary table of 2D airfoil lift characteristics

| | $\alpha_{stall}$ [deg] | $\alpha_o$ [deg] | $C_{l_\alpha}$ | $C_{L_{max}}$ |
|---|---|---|---|---|
| S5020 | 12.191 | -1.085 | 6.055 | 1.3032 |
| MH-45 | 13.346 | -0.621 | 6.086 | 1.3096 |
| MH-60 | 12.249 | -0.699 | 6.004 | 1.2559 |

The moment coefficient ($C_M$) is used as the main differentiating factor in design. Referring to Equations 2.1 – 2.2, the z and x directions of force can be combined and the moment arms added to determine the total moment equation about the center

of gravity. This equation is used extensively in longitudinal stability calculations to follow.

$$0 = C_m + \frac{x_w}{\bar{c}} C_N + \frac{x_p}{\bar{c}} C_{Np} + \frac{z_w}{\bar{c}} C_A + \frac{z_p}{\bar{c}} C_T \qquad (4)$$

All forces are nondimensionalized by the dynamic pressure ($q = \frac{1}{2}\rho v^2$)and planform area S, through the relation $C_x = \frac{X}{qS}$, where X is a flight force. Because the induced longitudinal moment of the plane (M) is not a function of wing distance from the center of gravity, and is generally in the nose-down direction [5], the minimization of the moment coefficient is the most useful way to reduce required control surface deflection for level flight (trim).

The S5020, a low Reynolds number self-stable airfoil, was determined to be the best airfoil due to its relatively small moment coefficient at low angles of attack (Figure 9). The minimization of the moment coefficient potentially eliminates wing twist and decreases manufacturing complexity and thus cost. All subsequent analysis will use the S5020 airfoil.

## 2.3 Analytical Solution to Finite Wing Properties

To ensure that the wing sizing is correct for the client-specified speed, a simple lift curve approximation can be used. The calculated lift curve slope for the S5020 at a chord-averaged Reynolds number of 500,000 is 6.055 $rad^{-1}$. Using the well-known lift-curve slope equation

$$a = \frac{a_0}{1+\frac{a_0}{\pi A e}} \qquad (5)$$

where the subscript "o" refers to the 2D characteristics, the 3D lift characteristics can be estimated. For an estimated efficiency of 0.95 (a quantitative design goal to increase plane endurance) and an aspect ratio of 6, the lift curve slope is calculated to be 4.52 $rad^{-1}$.

The required lift coefficient can be calculated as

$$C_L = \frac{2W}{\rho v^2 S} \qquad (6)$$

where S is simply determined by the aspect ratio and wing span of 72 inches (Table 2). For a 25 kt flight speed, and estimating a 10 lbf total plane weight, the required α for flight at 10,000 ft is 10.9 degrees. Because of the high α, a portion of the preliminary design process should be devoted to reduction in the total required incidence angle. This is covered extensively in the drag minimization section of Chapter 3.

### 2.3.1 Initial Sweep Angle Determination

Wing sweep is used in the low Reynolds number regime primarily to make the vehicle longitudinally stable in level flight. The initial plane sweep angle is determined by assuming that the plane aerodynamic center (AC) in the chord-wise direction can be found using a linear approximation

$$\frac{x_{ac}}{c} = 0.25 + \frac{m_o}{a_o} \qquad (7)$$

For the S5020, the AC is located at 24% of the chord length aft of the airfoil leading edge. To satisfy general pitch stability criteria, the static margin must be placed between 0.1$\bar{c}$ and 0.25$\bar{c}$ fore of the plane neutral point. CG travel of ±7% is required by the FAA at 14 CFR §23.21(b). A nominal static margin of 0.18 $\bar{c}$ meets both criteria.

To move the AC aft, and allow for a pusher configuration, a preliminary leading edge sweep angle of 30 degrees is chosen. The wing sweep angle for static stability is calculated in more detail in the preliminary design section in Chapter 3.

### 2.3.2 Initial Wing Cross Section Determination

To ensure that the wing is able to withstand the loading at the root, a bending moment calculation can be performed with the assumptions illustrated Figure 5. Assuming the wing lift distribution is elliptical [12], the moment on the wing root is given by

$$M = \frac{4}{3}\pi\left(\frac{b}{2}\right)nF \qquad (8.1)$$

where F is the force applied to the wing and n is the FAA required structural load factor. Simplifying for a wing half-span with the wing carrying the total weight of the plane

$$M = \frac{\pi bnW}{3} \qquad (8.2)$$

Applying this result to the bending stress equation $\sigma_{ut} = \frac{Mz}{I}$ where z is defined in Figure 3.

$$\frac{\sigma_{ut}}{n} = \frac{\pi bW(z_{max} - \bar{z})}{3I} \qquad (8.3)$$

For a wing having a 10 lb total weight, an initial chord length of 19 in, and a flight speed of 25 kts, the required wing moment of inertia must be at least 0.0461 $in^4$ if quasi-isotropic carbon fiber material properties from [16] are assumed.

To obtain this moment of inertia, three initial cross sections are explored in this thesis: a built-up wing consisting of carbon fiber spars, D-box, and ribs;

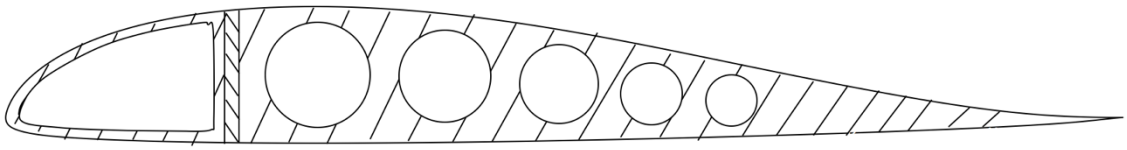

Figure 10. Built-up wing cross section for an S5020 wing

a semi-monocoque wing consisting of stringers and formers to maintain the wing skin loading;

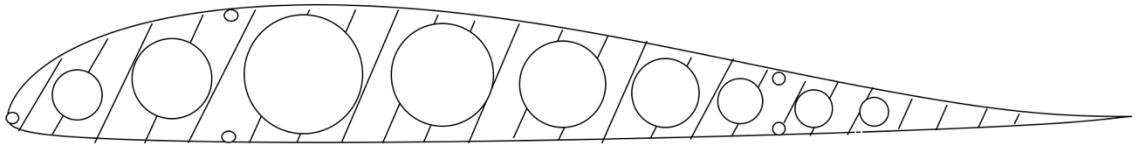

Figure 11. Semi-monocoque wing cross-section for an S5020 and a foam-filled wing.

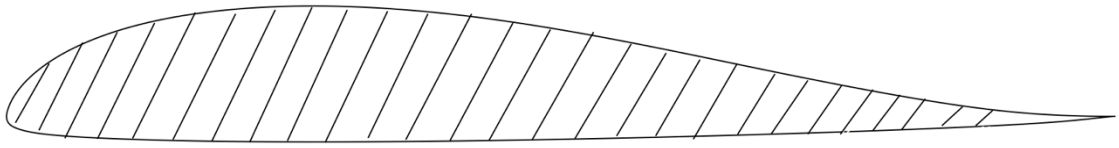

Figure 12. Foam-filled wing cross section for an S5020 wing

The primary difference between the cross sections in Figures 10 and 11 are the number of ribs or formers, and the size of the spar or stringer. The cross-sections are then evaluated against each other based on a simple weight ratio (oz/in), and potential manufacturing cost considerations. Due to the high weight of a foam-filled wing, as well as the cost associated with not reusing the foam in molding, this option

was not further explored. To reduce the total plane weight, the semi-monocoque wing is the best choice to analyze in further design steps.

## 2.4 Initial Plane Design

The initial planform of the Project UAS can be seen in Figure 13. The design features a simple pusher configuration and nose section with an on-board camera for first person view (FPV). The vehicle meets all qualitative constraints of the design listed in Table 2, except the wing span. This was determined to be non-essential to the design by the client.

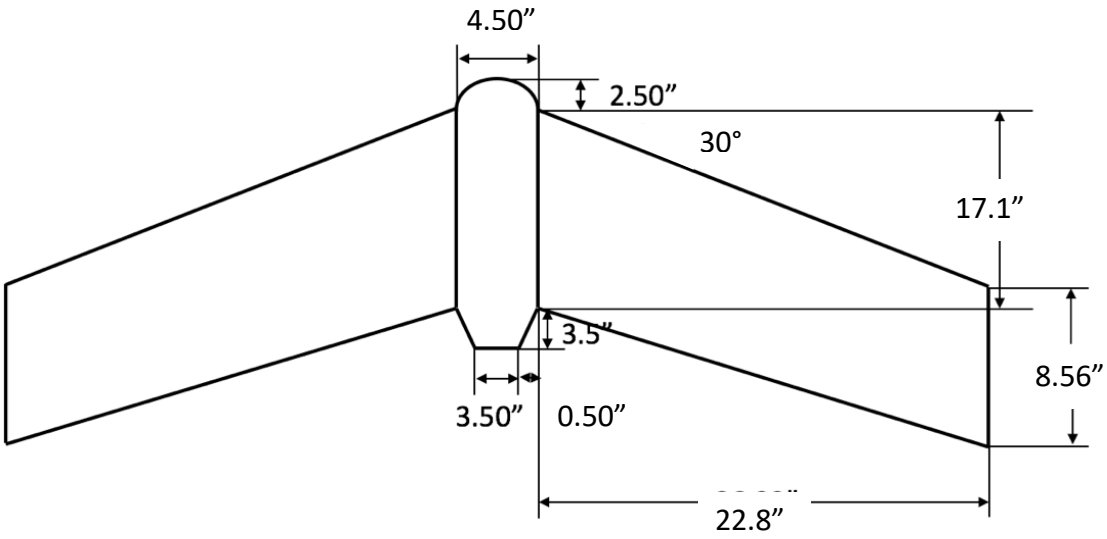


Figure 13. Preliminary plane design

Improvements to the design planform include total drag, total moment, and plane stability. The preliminary design process in Chapter 3 outlines the analytical solutions and specific design equations that led to a more refined design.

# Chapter 3. Preliminary Design Calculations

Given an initial design (Figure 13), this chapter outlines analytical and numerical analysis performed to decrease power consumption and total structural weight, and to increase static stability from the initial design iteration. The analysis in this chapter is presented in order of the plane design process presented in Section 1.3. The primary analysis performed is the reduction of drag on the wings, and determination of the stability characteristics of the vehicle. The results from this analysis will determine the flight regimes for the vehicle and the load factors required for structural analysis. Analytical solutions from references [4], [5], and [6] are used for the primary flight mechanics analysis considered in this chapter. When necessary, geometry-specific numerical solutions are used, but are checked for feasibility by comparing to theory.

## 3.1 Flight Mechanics and Aerodynamic Analysis

The flight mechanics in this section focus heavily on determination of flight forces, and wing drag reduction. These forces are then combined with stability equations to determine the control surface deflection necessary to achieve balance, or trim.

### 3.1.1 Wing Drag Minimization

The endurance limit (total flight time) and vehicle maximum range depend heavily on the minimization of drag. To maximize the range, the total drag force must be minimized [6]. In this analysis, the drag force (Equation 9.1) is the objective

function that will be minimized locally based on geometric and flight parameters listed in Table 4. The drag equation is

$$D = \frac{1}{2}\rho_\infty u_\infty^2 S(C_{Do} + C_{Di}) \qquad (9.1)$$

where the drag coefficient is split into two components: lift-induced drag ($D_i$), and zero-lift drag ($D_o$).

For optimization, boundaries on the flight speed, altitude, and flow parameters are set by the region, client, and guidelines from Reference [6] (Table 4). To reduce the total computation space, an Oswald efficiency factor goal of over 0.95 is set. A proposed method in Reference [7] allows the estimation of a theoretical Oswald efficiency factor (e), using the equation

$$e_{theo} = \frac{1}{1+f(\lambda-\Delta\lambda)A} \qquad (10.1)$$

where

$$f(\lambda - \Delta\lambda) = 0.0524(\lambda - \Delta\lambda)^4 - 0.15(\lambda - \Delta\lambda)^3 + 0.1659(\lambda - \Delta\lambda)^2 - 0.0706(\lambda - \Delta\lambda) + 0.0119 \qquad (10.2)$$

and

$$\Delta\lambda = 0.375 + 0.45e^{0.0375\phi_{25}} \qquad (10.3)$$

Here $\phi_{25}$ is the wing quarter-chord sweep angle and $\lambda$ is the taper ratio.

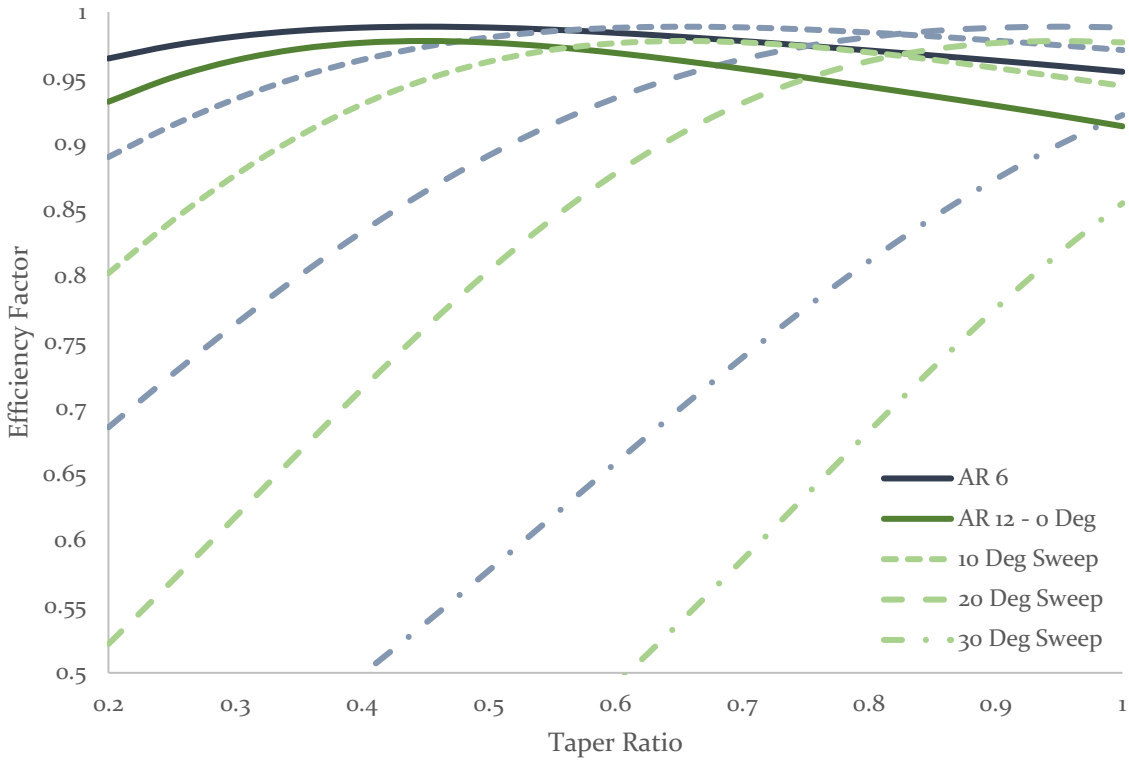


Figure 14. Effect of wing sweep and aspect ratio of a finite wing on theoretical Oswald efficiency

To meet the efficiency goal of 0.95 or higher, the sweep angle must be under approximately 25 degrees. For simplicity, 20 degrees is chosen, and thus the taper ratio ranges are 0.65 to 1.0. All optimization constraints and fixed parameters are listed in Table 4.

Table 4. Drag minimization constraints on optimization space

| Variable | Minimum | Maximum | Unit |
|---|---|---|---|
| Re | 100,000 | 1,500,000 | -- |
| A | 6 | 10 | -- |
| $\lambda$ | 0.65 | 1 | -- |
| $\phi_{25}$ | 20 | | deg |
| $\rho_\infty$ | 0.0023769 | | slug/ft$^3$ |
| $\mu$ | $3.82 \times 10^{-7}$ | | lbf-s/ft$^2$ |
| W | 10 | | lbf |

The boundaries on aspect ratio and taper ratio are the boundaries of concern in this analysis, creating a two-dimensional design space. To ensure that the vehicle stays within the low Reynolds number regime, a constraint on the Reynolds number is imposed. Because the vehicle is primarily used in the Gulf South region, the air properties are set at standard temperature sea-level. The weight of the plane is set at 10 lb in the conceptual design in Chapter 2. Aspect ratio ranges are set by convention from [6]. Using these boundaries, the wing geometry was determined using sequential least squares programming (SLSP) in SciPy. The embedded functions presented in Table 5 were used in addition to the objective function in the SLSP solution. Additionally, this allowed for all flow parameters and the wing geometry to be solved simultaneously.

Table 5. Local drag minimization embedded functions

| Formula | Definition | Source |
|---|---|---|
| $\mathbf{S = \frac{b^2}{A}}$ | Wing Area from AR | Phillips |
| $\mathbf{C_L = \frac{2W}{\rho_\infty v_{MD}^2 S}}$ | Required Lift Coefficient | Derived |
| $\mathbf{C_{Di} = \frac{C_L^2}{\pi A e}}$ | Induced Drag | Phillips |
| $\mathbf{v_{MD} = \left(\frac{4}{\pi A e C_{Di}}\right)^{1/4} \sqrt{\frac{(W/S)}{\rho}}}$ | Minimum Drag Speed | Phillips |
| $\mathbf{c_r = \frac{S}{b(1+\lambda)}}$ | Derived Root Chord | Derived |
| $\mathbf{c_t = \lambda c_r}$ | Tip Chord | Phillips |
| $\mathbf{Re_{min} = \frac{\rho_\infty v_{MD} c_t}{\mu}}$ | Reynolds Number | Anderson |
| $\mathbf{v_G = 33\sqrt{W/S}}$ | Planform Area | 14 CFR Part 23 |

Using the resultant geometry (λ = 0.811, A = 6.02), the zero-lift drag coefficient ($C_{D_0}$) is estimated as 0.01053. A summary of the solution geometry can be seen in Figure 15.

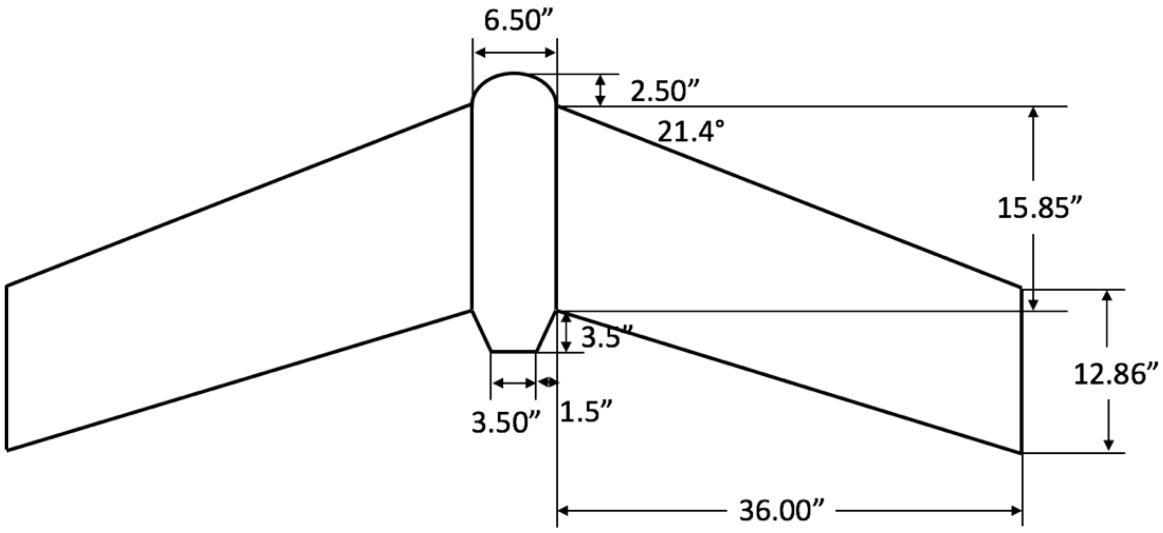


Figure 15. Basic planform geometry of Project UAS

To ensure that the vehicle minimum drag speed is accurate, the vehicle minimum drag speed $v_{MD}$ is checked by calculating the zero-lift drag ($D_o$) and the induced drag ($D_i$). For the geometry shown in Figure 15, the minimum drag speed is to be approximately 52 fps at standard sea level conditions.

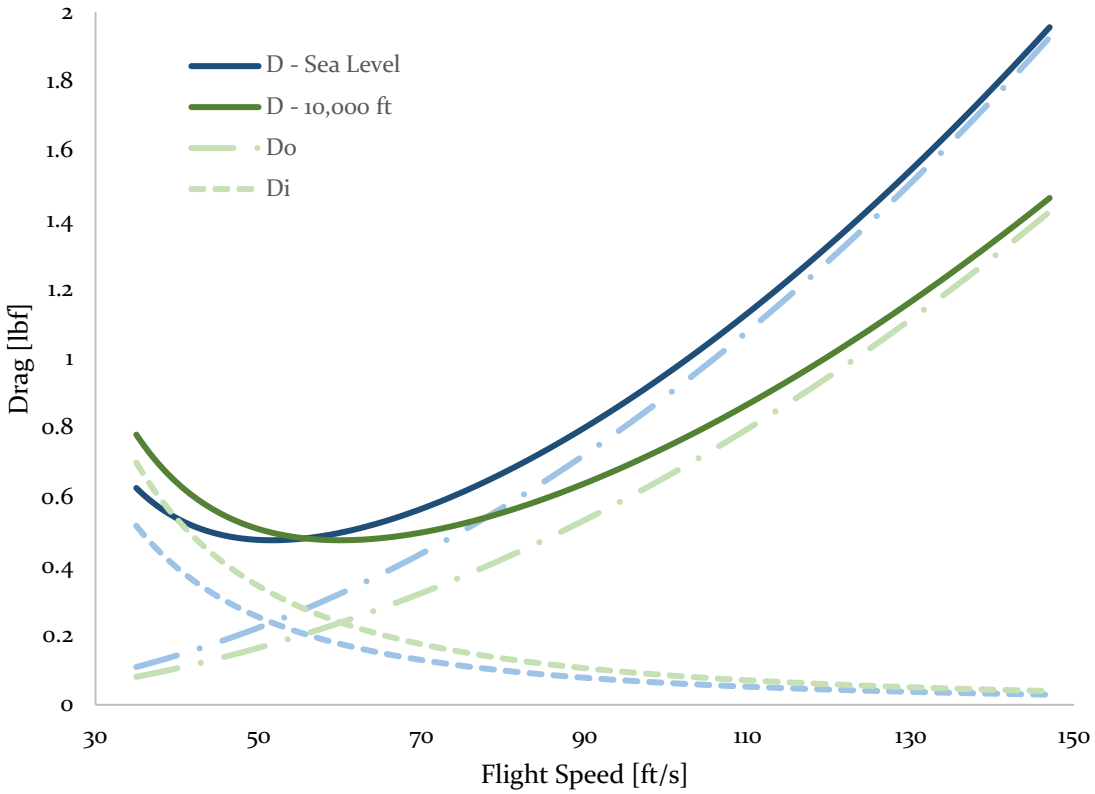


Figure 16. Drag buildup of zero-lift drag and induced drag for an intermediate design iteration

Figure 16 shows the entire flight regime from the stall speed of approximately 35 fps to the maximum legal ground speed of 100 mph, as set by 14 CFR Part 107 [2]. The minimum drag speed at sea level is approximately 52 fps, therefore, the solution is performed correctly. For the maximum altitude defined through a combination of 14 CFR Parts 23 and 107, 10,400 ft., the minimum drag speed is approximately 60 fps.

The solution to the wing geometry is the first step in the preliminary design process. In this thesis, this was performed using SLSP drag minimization. After this point, the vehicle must be balanced in the longitudinal plane.

### 3.1.2 Static Longitudinal Stability and Trim

Level flight of a plane is ensured by two parameters: balance (trim), and stability. Balance refers to the sum of total plane moments being zero about the center of gravity (Equation 11.1). Stability refers to the plane's ability to return to the intended flight path upon perturbation (Equation 11.2).

$$c_m = 0 \tag{11.1}$$

$$\frac{\partial c_M}{\partial \alpha} < 0 \tag{11.2}$$

There are two flight modes that are of concern, powered flight and gliding flight. As per FAA FAR Part §23.175, a plane is required to be balanced in powered flight. This will be addressed in detail in Chapter 4; however, the focus of this section is to balance the plane in gliding flight, and establish methods to determine powered stability.

Equation 10.1 can be expanded using the body-centered forces in Figure 3 to obtain Equation 4.

$$0 = \mathrm{C_m} + \frac{\mathrm{x}_w}{\bar{\mathrm{c}}}\mathrm{C_N} + \frac{\mathrm{x}_p}{\bar{\mathrm{c}}}\mathrm{C_{Np}} + \frac{\mathrm{z}_w}{\bar{\mathrm{c}}}\mathrm{C_A} + \frac{\mathrm{z}_p}{\bar{\mathrm{c}}}\mathrm{C_T} \tag{4}$$

All terms with subscript "w" refer to the distance from the total vehicle CG to the wing, and all terms with subscript "p" refer to the distance from the total vehicle CG to the propeller center of rotation. The mean aerodynamic chord ($\bar{\mathrm{c}}$) is used as the normalizing chord length in all balance equations.

To adhere to 14 CFR Part §23.21(b), a travel of ±7% of $\bar{\mathrm{c}}$, and referring to the general static margin guidelines for stability from [4], an initial static margin of 18%

yielded a location for the center of gravity 2.46 inches fore of the aerodynamic center line (Figure 17).

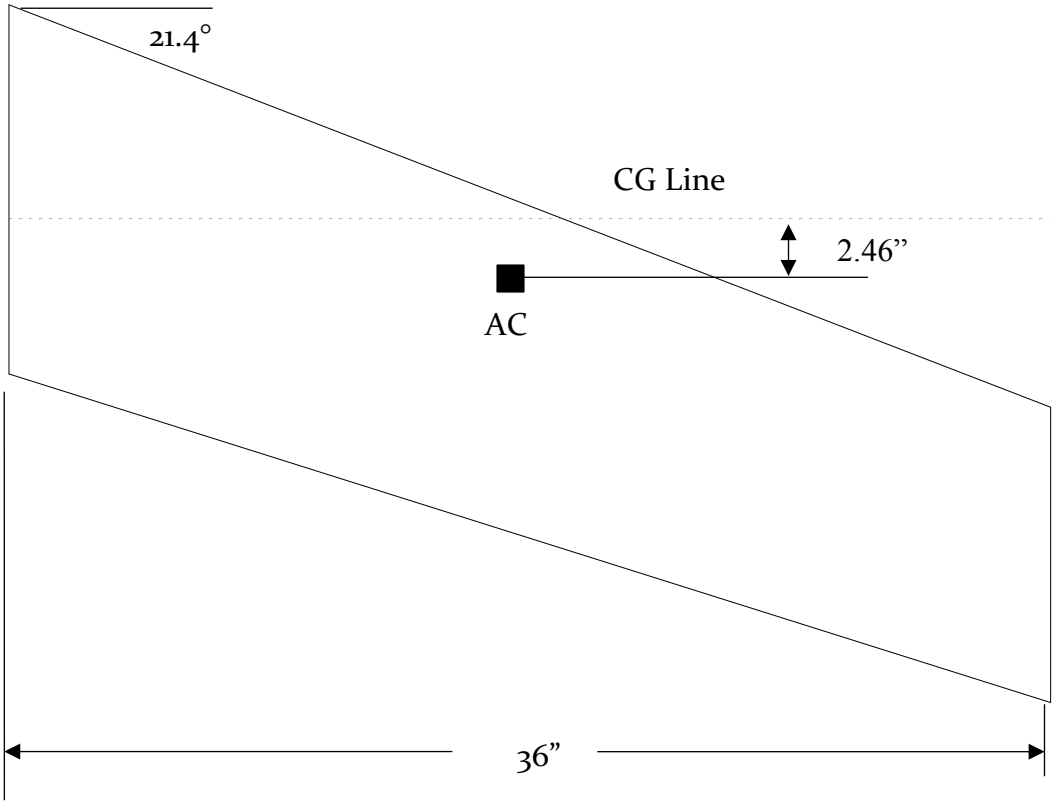


Figure 17. Swept cord of the aircraft

The plane itself, however, is still unbalanced in level flight. Therefore, the required control surface deflection for trim should be determined. This is often done by expanding Equation 4 to include control surface deflection derivatives (delta derivatives).

The stability derivatives of primary concern in this chapter are the alpha derivatives ($C_{x_\alpha}$) and delta derivatives ($C_{x_\delta}$), or the pitch and control surface deflection angle derivatives respectively. xflr v6.32 was used to first rotate each airfoil section by a single degree at 80% of the chord (common practice for initial

control surface design), and the 2D characteristics for each airfoil were determined from a Reynolds number of 100,000 to 1,500,000, the ranges of Reynolds numbers seen in Table 4 as the analysis boundaries. The lift curves in Figure 18 were determined at Re=500,000 corresponding to the mean aerodynamic chord of the UAV at the minimum drag speed.

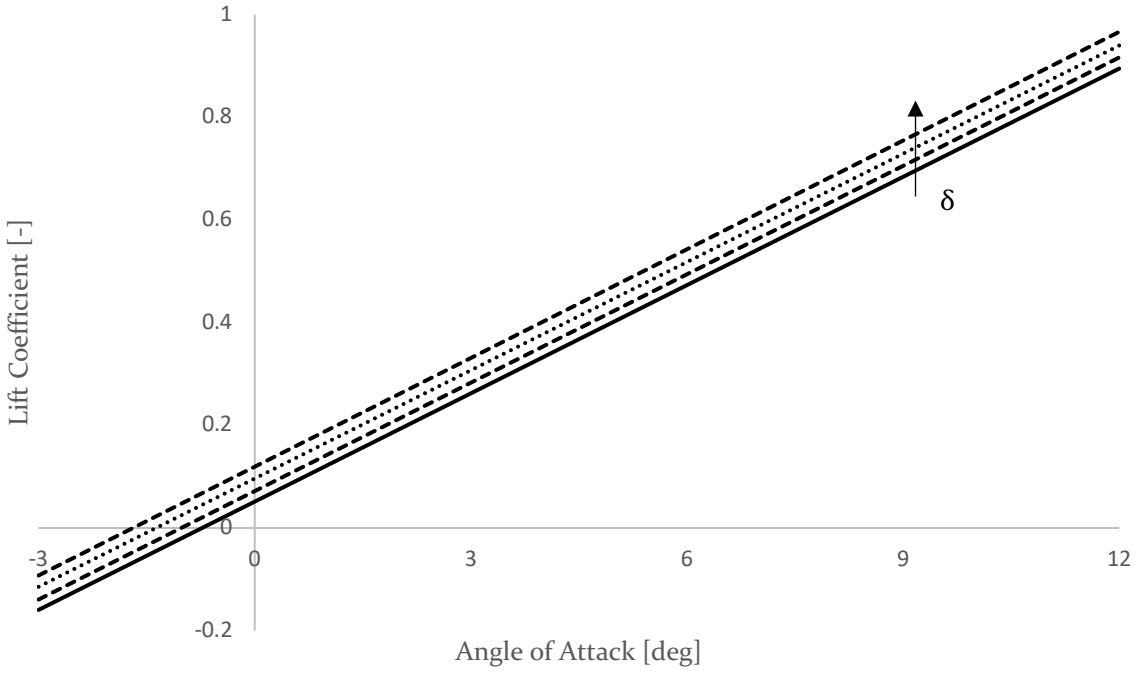


Figure 18. 3D VLM lift slope curves for $\delta$= 0,1,2,3

Comparing the curve to theory, the slopes of each curve are approximately the same, but the zero-lift angle of attack is shifted to be more negative, enumerated in Table 5.

Table 5. Delta derivative validation table

| Deflection [deg] | $\alpha_0$ [deg] | $C_{L_\alpha}$ [$deg^{-1}$] |
|---|---|---|
| 0 | -0.73 | 0.0703 |
| 1 | -1.02 | 0.0704 |
| 2 | -1.37 | 0.0703 |
| 3 | -1.69 | 0.0706 |

Recalling the initial statement of the total plane longitudinal trim relation in Equation 4, the total tailless equation for balance reduces to

$$0 = C_{m_w} + \frac{C_N}{\bar{c}} l_w + \frac{C_A}{\bar{c}} z_w \qquad (4.1)$$

due to the lack of force contributions from the powerplant. As a general guide, if the deflection required for trim allows for more than 5 degrees of elevon deflection before stall at 15 degrees, the gliding mode is considered stable. The contributions of the control surface deflection longitudinally can be expanded to the form using the correction from wind-centered coordinates to body-centered coordinates (Equations 1.1 – 1.2).

$$\sum C_m = C_{m_\alpha}(\alpha - \alpha_0) + C_{m_\delta}\delta +$$

$$\frac{x_w}{\bar{c}}\left[\left(C_{L_\alpha}(\alpha - \alpha_0) + C_{L_\delta}\delta\right)\cos\alpha - C_{D_\alpha}\sin\alpha\right]$$

$$+ \frac{z_w}{\bar{c}}\left[\left(C_{L_\alpha}(\alpha - \alpha_0) + C_{L_\delta}\delta\right)\sin\alpha + C_{D_\alpha}\cos\alpha\right] \qquad (4.2)$$

which takes into account both normal and axial forces, as well as the control surface deflection. For a level flight condition, the α terms become constants and the level flight moment coefficient can be set to the left-hand side. Giving

$$\sum C_m = C_{m_o} + \frac{x_w}{\bar{c}} C_{N_o} + \frac{z_w}{\bar{c}} C_{A_o} \qquad (4.3)$$

where the subscript "o" refers to the initial flight conditions. Combining Equations 4.1 and 4.3, the equation reduces to

$$C_{m_o} + \frac{x_w}{\bar{c}} C_{N_o} + \frac{z_w}{\bar{c}} C_{A_o} = C_{m_\delta}\delta + \frac{x_w}{\bar{c}} C_{L_\delta}\delta \qquad (4.4)$$

For the given flight conditions and geometry, the gliding trim angle (the angle where both sides of Equation 4.4 are equal) is found to be 9.7 degrees.

Safe limits for the center of gravity can be determined based on the ability of the plane control surfaces to right the plane under reasonable flight conditions. Using Equation 4.4, the FAA requirement of ±7% travel of the center of gravity can be explored by changing $x_w$. For a control surface deflection, δ, of 15 degrees, the corresponding maximum CG travel from nominal is 8.3% fore of the design CG. The CG travel limit in gliding flight, then, is met with no available aileron movement in gliding flight. A more physically realistic approach is necessary for performance estimation that includes the contributions of a propeller: the thrust and propeller normal force. This can be found in Chapter 4.

### 3.1.3 Static Directional Stability Analysis

Tailless planes are often prone to directional instabilities. This is most often due to the fact that there is no vertical surface to allow for side forces to correct non-nominal plane motions [5]. The restoring moment (N) is a component of the combined side forces (B) and moment arm from the planform CG to the point of application (Figure 3). For typical flight vehicles, the recommended restoring moment derivative range is between 0.06 and 0.15, corresponding to $1.05 \times 10^{-3}$ and $2.62 \times 10^{-3}$ $deg^{-1}$ respectively [6]. For a tailless plane; however, a restoring moment

coefficient of $3.33x10^{-4}$ $deg^{-1}$ is the absolute minimum [5]. This is less than that suggested for a traditional planform because there is no restoring component of the tail.

To increase the vehicle's ability to return to the original orientation, vertical surfaces are added. For a tailless plane, this can be done at the wingtips, at the fuselage, or some combination of the two. A representative case for each choice can be seen in Figure 19.

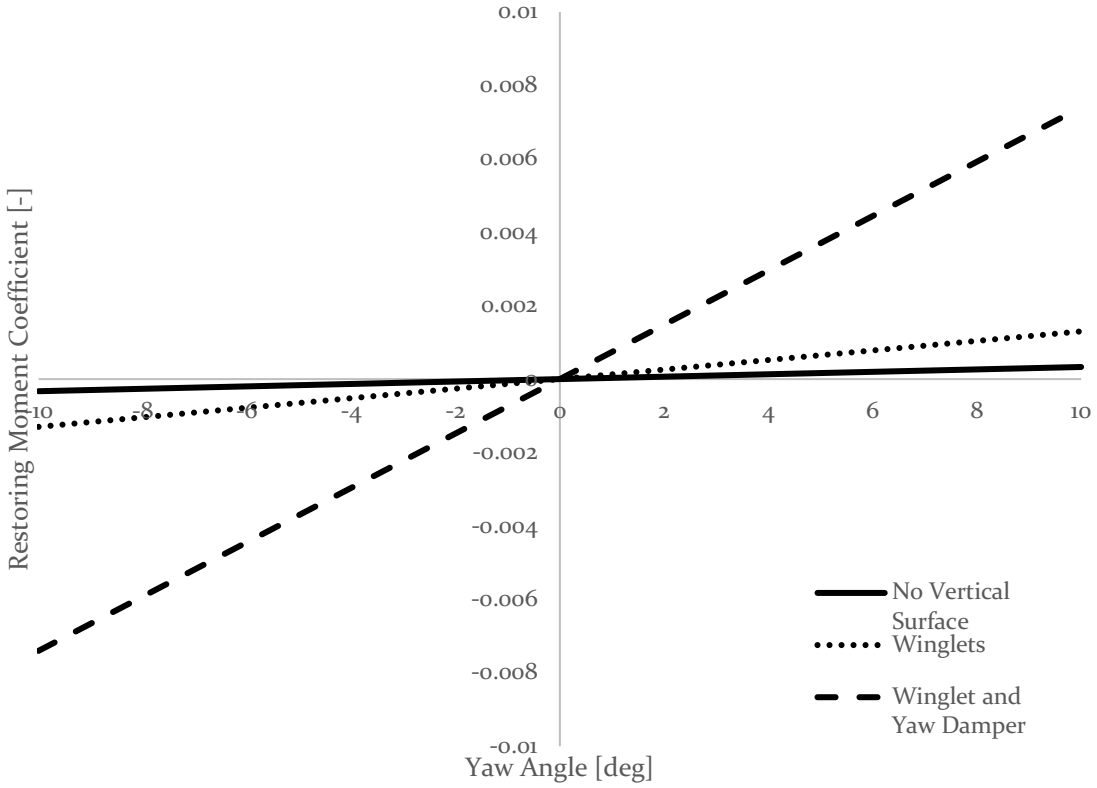


Figure 19. Restoring moment for various planform configurations

It is determined that winglets as well as yaw dampers at the fuselage should be added to allow for proper restoring moment under nominal conditions. A visualization of the wings and added vertical surfaces can be seen in Figure 20.

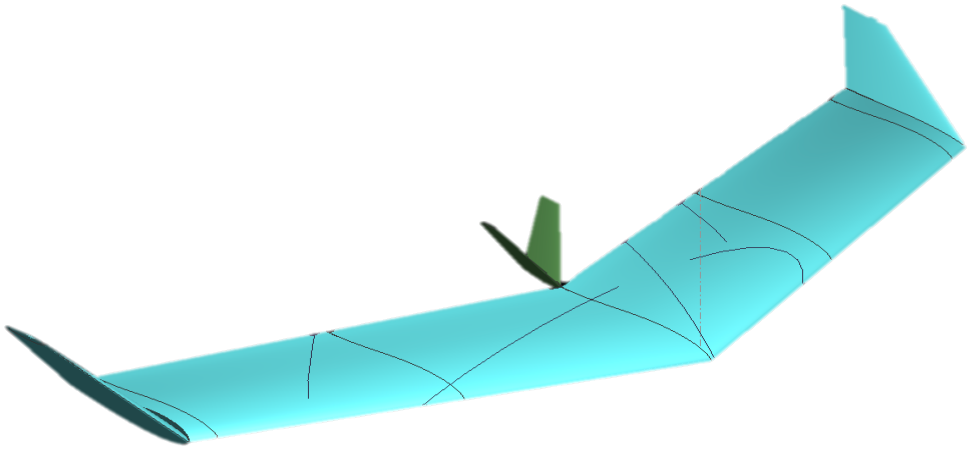

Figure 20. xflr visualization of Project UAS directional stability additions

### 3.1.3 Flight Envelope Determination

To determine the load limits required by 14 CFR Part 23.333, equations 12.1 and 12.2 should be evaluated and a flight envelope created. A flight envelope is a visual representation of the stall and structural load limits of the vehicle, and is used in structural analysis as flight limit loads, and stall points in flight mechanics. The determination of the flight envelope curve uses the stall equations

$$n_{max} = \frac{q}{(W/S)} C_{L_{max}} \qquad (12.1)$$

$$n_{min} = \frac{q}{(W/S)} C_{L_{min}} \qquad (12.2)$$

where the load limits $n_{max}$ and $n_{min}$ are set by 14 CFR Part §23.333 (Appendix B). The maximum and minimum lift coefficients are again estimated using the vortex lattice method in xflr v6.32. The limits of the coefficients are estimated as the angle of attack where the Kutta condition does not hold, corresponding in reality to flow separation about the finite wing. The left-most boundaries in Figure 21 correspond to these stall limits. The limit loads shown as the right-most boundaries correspond

to structural failure for a normal category plane defined by 14 CFR Part §23.333-§23.335. The load factor is defined as the load force divided by the weight and is roughly comparable to the g-force on the planform. The maximum structural limit that the plane is required to endure for the stated vehicle life is defined as +3.8 times the level flight force on the planform.

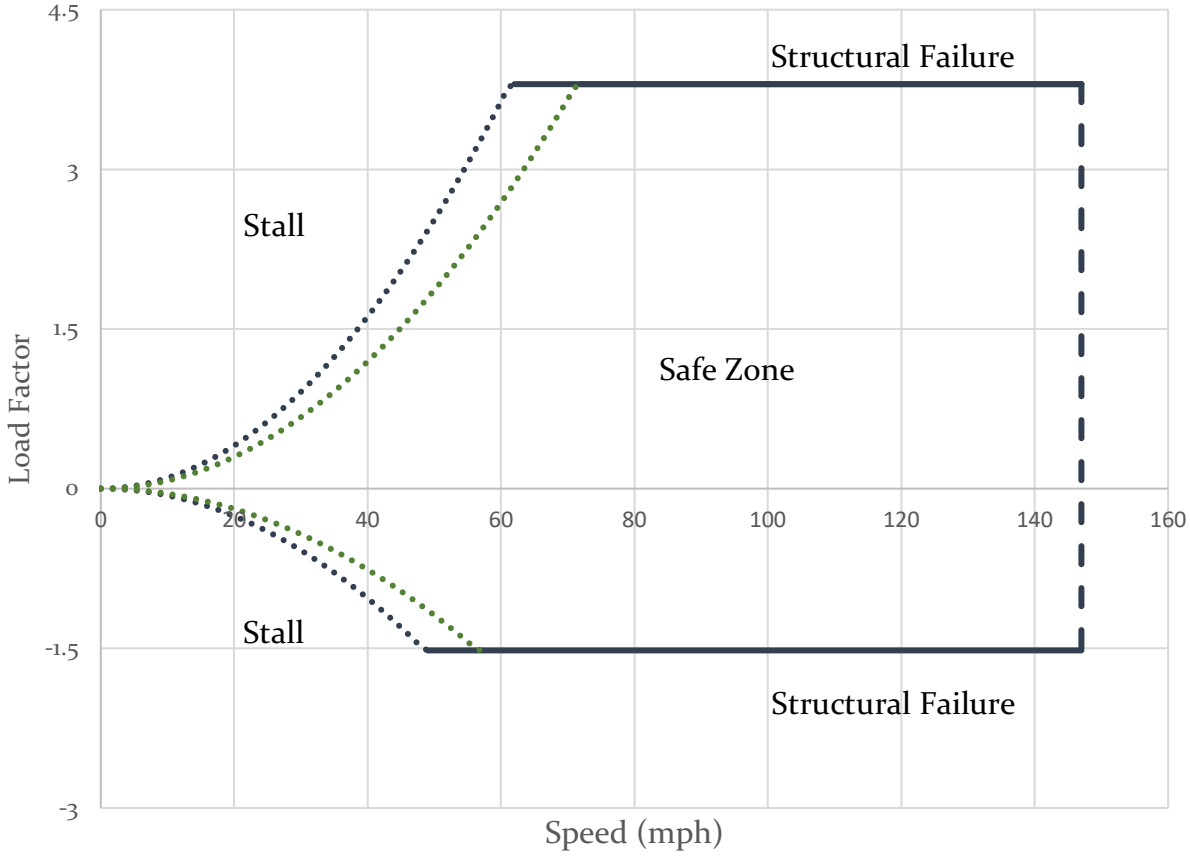


Figure 21. Estimated flight envelope at sea level and 10,000 ft

From Figure 21, it can be seen that the stall region increases with an increase in altitude. The stall speed equation

$$v_s = \sqrt{\frac{2W}{\rho_\infty S C_{L_{max}}}} \qquad (13)$$

shows that stall speed will increase with a decrease in density (a function of altitude). These load factors can then be applied to the wing-to-fuselage connection to design a sutible internal substructure.

## 3.2 Structural Analysis

The most common structural failure modes are addressed in this section: maneuvering limit loading, and landing. These modes tend to have the highest stresses in fuselage. This section follows the load path from the fuselage frame outward to the wings.

### 3.2.1 Fuselage Frame Design

To reduce the total skin deflection at the fuselage connection during loading, a rib section is connected to the fuselage frame. This configuration is analyzed as the limit loading applied directly to the frame. A full frame interior payload section can be seen in Figure 22. A worst-case analysis of one connection remaining in a maneuver is shown in Figure 23.

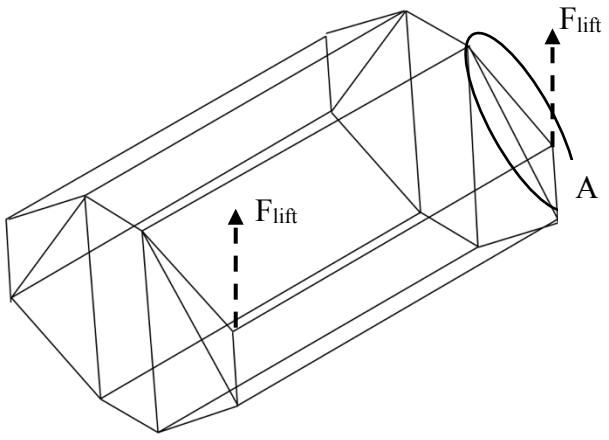


Figure 22. Frame payload section with max stress component highlighted

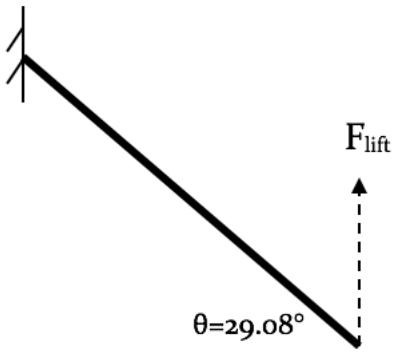


DETAIL A

Figure 23. Free body diagram of fuselage frame section with full half-lift load applied

Assuming the bending stress and the compressive stress are additive, the general stress equation (Equation 3.1) becomes

$$\frac{\sigma_{ut}}{n} = \frac{My}{I} + \frac{F}{A_c} \qquad (14.1)$$

where $A_c$ is the frame tube cross-section. Referring to the free body diagram in Figure 23

$$\frac{\sigma_{ut}}{n} = \frac{Wl\cos\theta\sin\theta r_o}{2\left[\frac{\pi}{2}(r_o^4 - r_i^4)\right]} + \frac{W\sin\theta}{2\pi(r_o^2 - r_i^2)} \qquad (14.2)$$

and using commercially available unidirectional carbon fiber tubing from [17], with properties from [16], the safety factor is determined to be 3.88. This exceeds the safety factor of 1.5 required by 14 CFR 23.335.

Bending analysis and strength analysis were performed to verify that the frame can support a landing load. D'Alembert's principle can be used to find an equivalent load factor for dynamic frame design [19]. The recommended load factor of 2.6 is applied to the points seen in Figure 24.

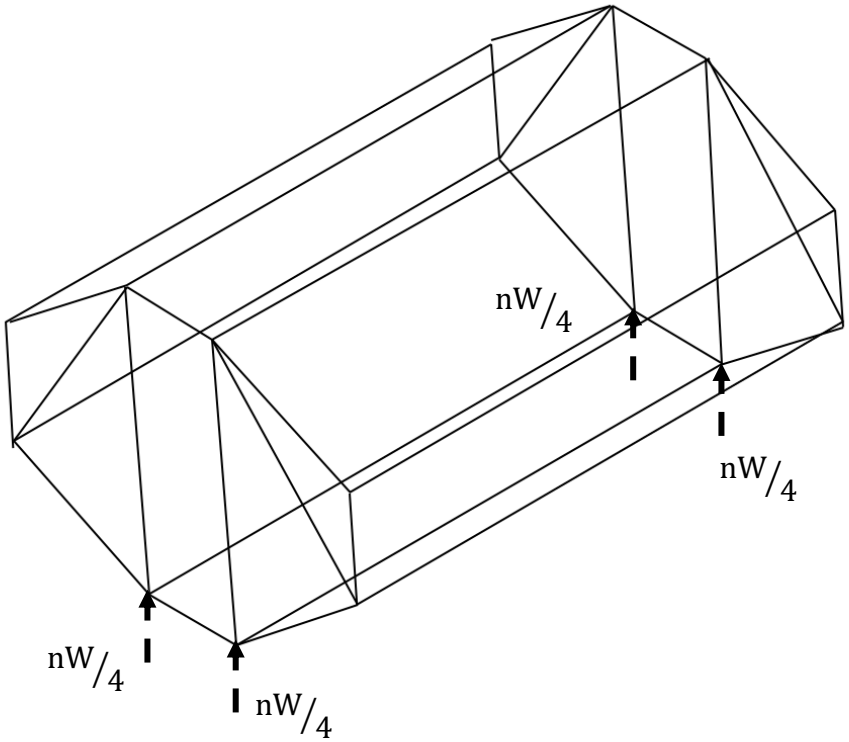


Figure 24. Landing load locations on the payload fuselage section

It is assumed that the landing gear applies four equivalent loads onto the frame. A similar process to that used in Equation 14.2 applies a quarter-mass model to Equation 13.1. The equation can be expanded to the form

$$\frac{\sigma_{ut}}{n} = \frac{W l \cos\theta \sin\theta r_o}{4\left[\frac{\pi}{2}(r_o^4 - r_i^4)\right]} + \frac{W \sin\theta}{4\pi(r_o^2 - r_i^2)} \qquad (14.3)$$

the maximum distance for the application of this landing load is 7.67 inches. Because the length of the payload section is less than twice this distance, the design inherently meets this loading criterion. At this point in the analysis, the structure of the wings themselves should be considered.

### 3.2.2 Wing Stress Simplification

The main loads on any wing are the lift, drag, and induced pitching moment. Lift can be shown to be a bending stress in the span-wise direction. The pitching

moment on a wing is a function of the moment coefficient and is applied in the 2D chord-wise plane. The drag on a plane wing is applied as a bending moment to the chord-wise direction. For this analysis, lift and drag are resolved to normal and axial forces seen in Figure 3.

VLM in xflr v6.32 was used to determine the span-wise lift distribution shown in Figure 25. A 6$^{th}$ order polynomial was curve fit to the lift load with an $R^2$ value greater than 0.99. This polynomial was integrated using cantilever beam boundary conditions at the root, with no deflection or deflection angle, to determine the lift-induced moment curve along the wing span.

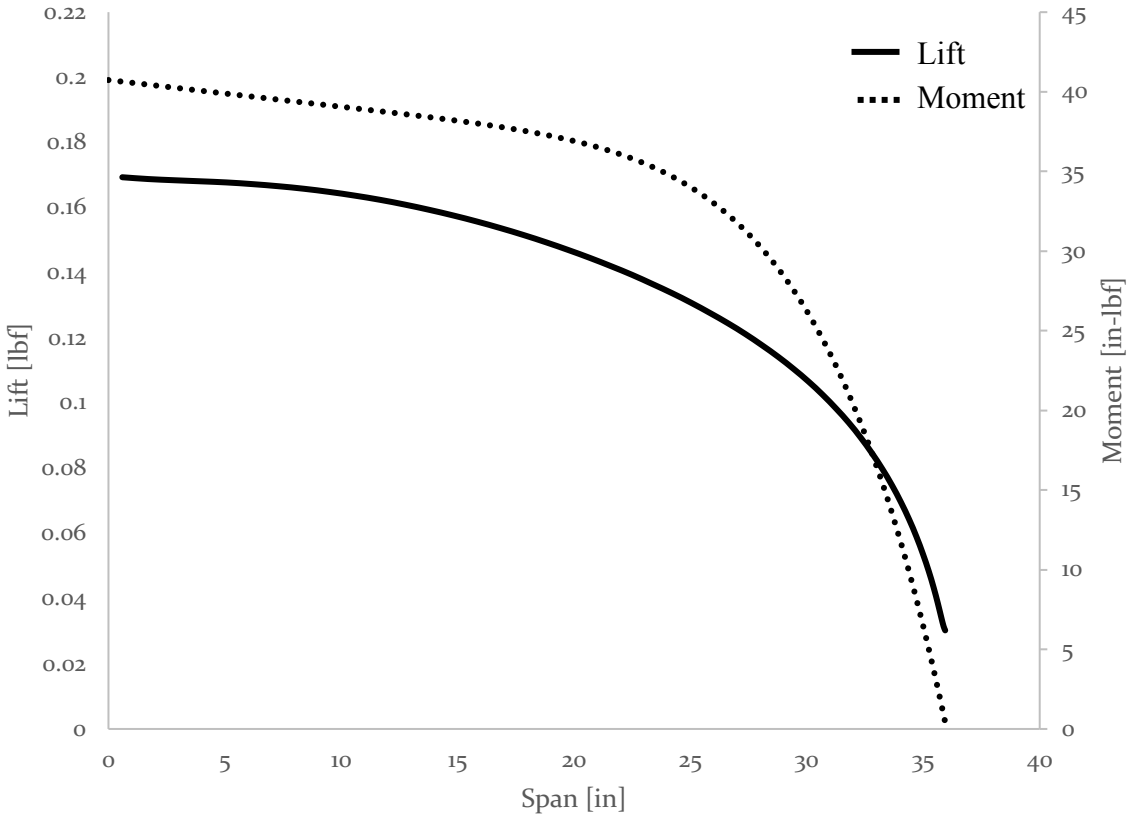


Figure 25. Lift and moment spanwise distribution for an intermediate design iteration

Integrating the lift curve along the half-span, the total lift is determined to be 5.01 lb, compared to the 5.00 lb in theory. The net integrated moment on the wing is, then, 153 in-lb.

The second stress on the wing is the drag-associated stress. This is determined, again, using VLM. From Figure 26, it can be seen that the force values are orders of magnitude less; however, the stresses are shown to demonstrate negligibility in future analysis.

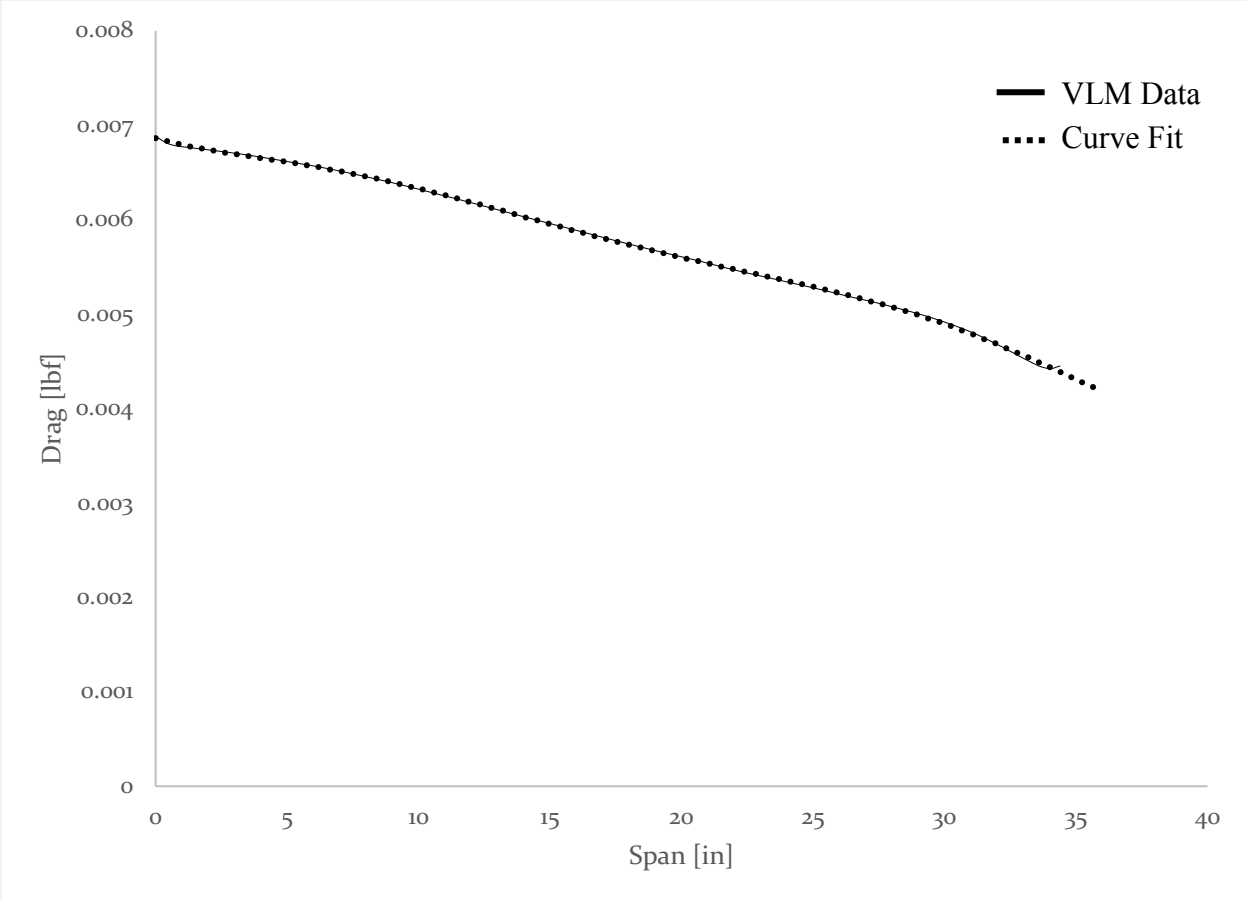


Figure 26. Drag spanwise distribution for an intermediate design iteration

From an integration of the spanwise drag curve in Figure 26, the total drag is approximately 0.202 lb, and the point of application can be estimated to be 16.71

inches from the wing root. This corresponds to a moment of 3.37 in-lb. The stresses on the wing root are dependent on the wing cross section, as well as the spanwise force distribution. The stresses are calculated at the wing root using a moment of inertia tensor determined from SolidWorks 2017 as

$$I_{ij} = \begin{bmatrix} 0.15 & 0.16 & 0.00 \\ 0.16 & 4.91 & 0.00 \\ 0.00 & 0.00 & 5.06 \end{bmatrix} \text{in}^4$$

The moment of inertia tensor refers to a 0.004" skin thickness at the wing root – the thinnest feasibly available carbon fiber fabric available from [19].

The pitching moment stress can be determined as

$$\tau = \frac{Tz_{max}}{J} \qquad (15.1)$$

where the torque (T) on the wing is simply the induced pitching moment (M). The maximum distance is simplified in this chapter to $\frac{1}{2}(t/c)c_r$ where $c_r$ is the root chord. This distance approximates the centroid distance at the maximum thickness. The polar moment of inertia (J) was determined in SolidWorks 2017 to be 5.06 $\text{in}^4$. Applying these changes to the equation and using the pitching moment relation $M = \frac{1}{2}qC_M S\bar{c}$ [6], the equation becomes

$$\tau = \frac{qC_M S\bar{c}(t/c)c_r}{4J} \qquad (15.2)$$

using the values from an intermediate design iteration, the calculated value of torsional stress is 1.61 psi. A summary of each of the stresses on the wing root is given in Table 6.

Table 6. Stress summary table

| **Principal** | **Stress [psi]** | **FoS** |
|---|---|---|
| Lift Induced | 41.5 | 2000 |
| Drag Induced | 0.887 | 93000 |
| Pitching Moment Induced | 1.61 | 8100 |

Because the lift induced stress is orders of magnitude higher than the drag and pitching moment stresses, this is used in all future design calculations. FEA on the wing skin in Chapter 4 will attempt to reduce the factors of safety to a reasonable engineering level.

### 3.2.3 Analytical Stringer Sizing

A stringer in this design refers to thin span-wise members that primarily keep the wing shape similar to a traditional wing spar (Figure 11). Primary stringer sizing is done to minimize the wingtip deflection in flight. To avoid significant change in the load distribution and adhere to 14 CFR Part §23.201(c), the stringers must be able to provide enough rigidity to not significantly change the vertical location of the CG under worst-case loading. Utilizing the load distribution given in Figure 25, the simple bending equation can predict the wing vertical deflection.

$$EI\frac{\partial^2 z}{\partial y^2} = L'(y) \qquad (16)$$

In this equation, z is the wing deflection upward, y is the span-wise position, and L'(y) is the lift per unit span as a function of the span. The stringer can be modelled

as a cantilever beam with zero deflection at the fuselage connection, and zero deflection angle at this point.

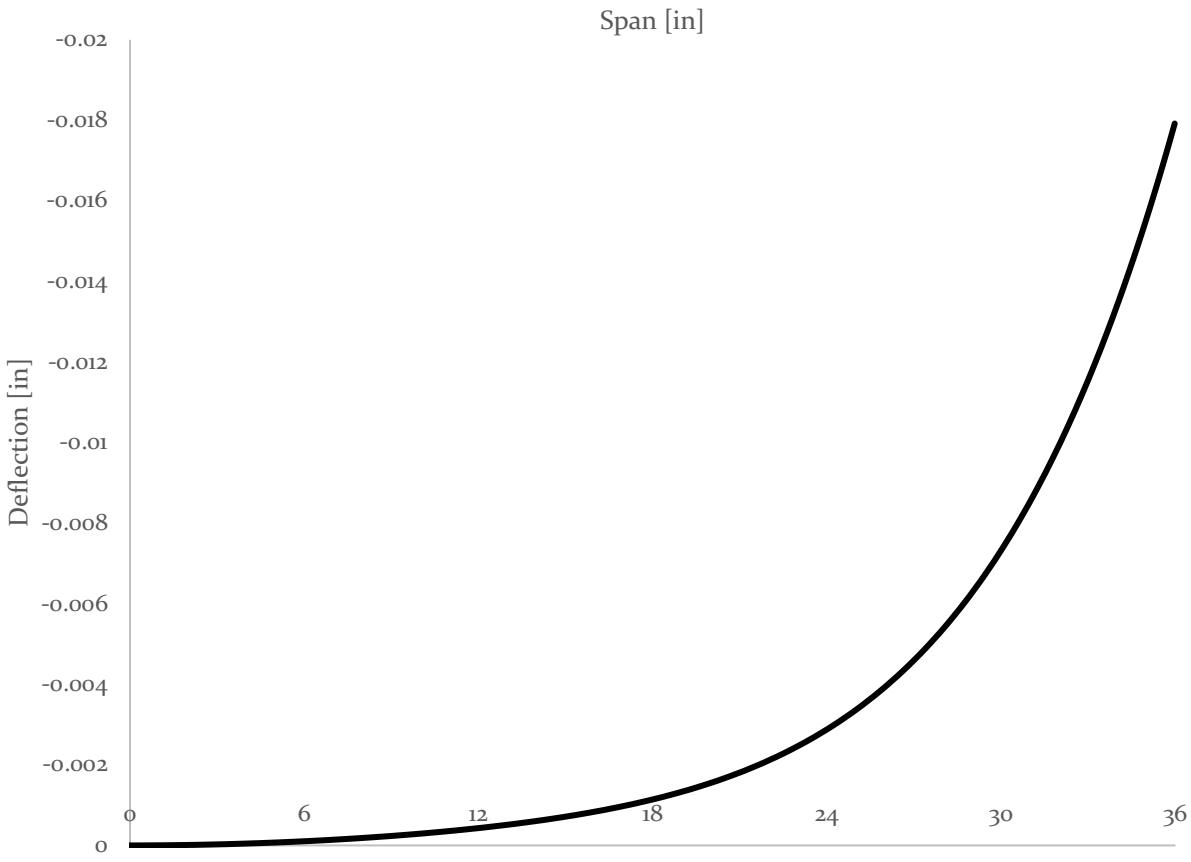


Figure 27. Pure spar loading deflection curve

From Figure 27, it can be seen that the maximum wingtip deflection, assuming a carbon fiber stringer takes the entire load [17], is less than 1/32", or 0.03 degrees. Therefore, there will not be an appreciable change in the center of gravity at this maximum loading scenario. Due to the low change in CG location, detailed analysis is simplified to exclude aeroelastic effects.

Once the plane is structurally designed, the total weight can be revised. Using an estimate in SolidWorks, the current design iteration has less than 1 lb of

structural weight. From this total plane payload and structural weight of approximately 6 lb, a powerplant can be selected.

## 3.3 Powerplant Selection

The powerplant selection is highly dependent on the weight of the plane to increase the thrust to weight ratio for hand launch and the power required to increase the total vehicle endurance. The dynamic behavior of a clean propeller (a propeller at the leading edge of the fuselage) informed basic propeller selections for the design. Though the propeller is not exposed to the clean freestream in a pusher configuration, propeller blade theory used in the code will predict an approximate value for the power plant and propeller required. Because the design configuration tends to have lower dynamic thrust, the analysis in this section will yield and oversized result that is reduced in practice.

### 3.3.1 Power Required

The power required, $P_R$, is defined as that needed to overcome planform drag, or $P_R = Dv$. Neglecting the contribution of the fuselage, and combining Equation 9.1, the power is

$$P_R = \frac{1}{2}\rho v^3 \left(C_{D0} + \frac{C_L^2}{\pi e A}\right) \qquad (17)$$

The FAA requires that all vehicles be able to take off from a density altitude of zero to 10,000 ft [1]. The power required at each density altitude is shown in Figure 28.

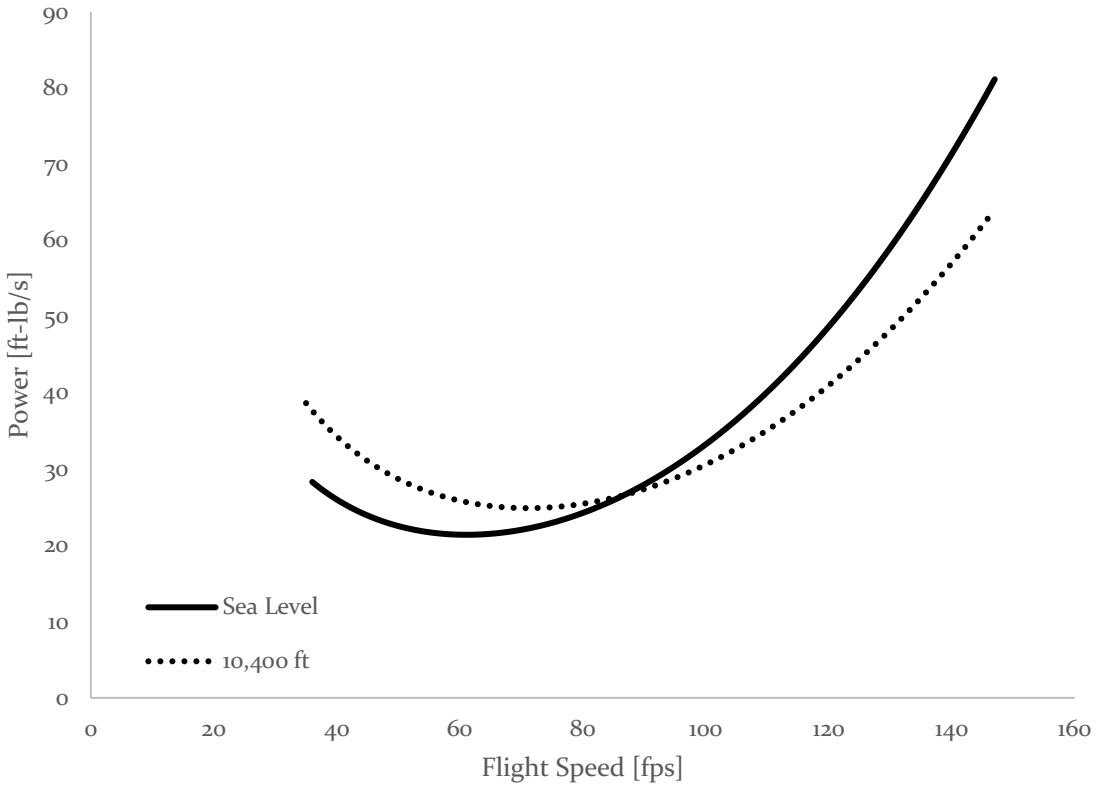


Figure 28. Power required at sea level and 10,000 ft

The minimum power speed was calculated to be approximately 60 fps. 14 CFR Part 107 limits the flight ceiling of a UAV to 400 ft. However, 14 CFR §23.45 requires that the vehicle be analyzed at 10,000 ft. The maximum gust velocity required by 14 CFR Part §23.333 corresponds to a 50 fps gust at cruise, $v_C$. Therefore, the propeller must be able to supply power at 10,400 ft up to this point; however, the vehicle is not required to accelerate at gust velocity, $v_G$. A sample power comparison between the power available ($P_A$) for a 10x6-4 propeller, and the power required ($P_R$) is shown in Figure 29.

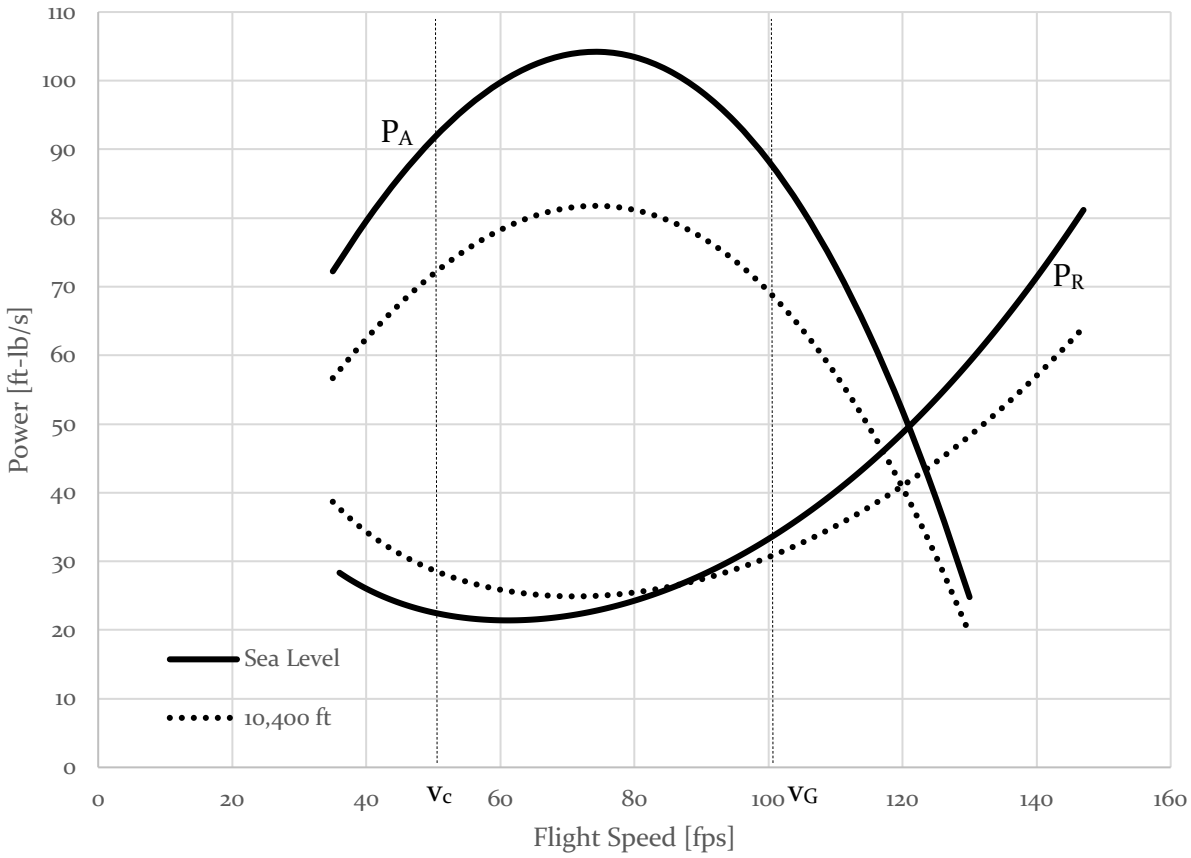


Figure 29. Power budget curves for all physical and legal flight regimes

For all points in the flight envelope, a clean 10x6-4 propeller is sufficient to provide the required power at all relevant design speeds. A 10x6-4 propeller, further, remains under the 0.8 BHP limit of the engine by approximately a factor of two [19], and corresponds to an approximate 5.6 lbf static thrust.

### 3.3.2 Fuel Required Determination

To determine the final weight estimate at this stage in the design process, the fuel weight is estimated. Assuming an average engine efficiency of 30%, the required fuel weight can be easily determined from performance data given in the previous section. The fuel weight can be quickly estimated by

$$w_{fuel} = \frac{Dvt/\eta_{eng}\eta_p}{E_{fuel}} \quad (18)$$

where $E_{fuel}$ is the stored chemical energy in gasoline. Setting cruise to the minimum power speed, $v_{MP}$, the required gas weight for a three-hour flight time is 0.071 lb of fuel [8]. A propeller efficiency at this speed is calculated using propeller blade theory to be 0.68.

## 3.4 Interim Design Overview

The preliminary design phase led to a total decrease in zero-lift wing drag of 27% and wing moment of 80% with respect to the initial iterations shown in Figure 13. In this phase, winglets and fuselage yaw dampers were added to the UAV planform to allow for better lateral stability. The detail design process is required to determine the powered stability criteria, and determine the final weight distribution of the plane.

# Chapter 4. Detail Design Calculations

The following chapter entails the numerical models and analysis done to improve the Chapter 3 design. The numerical tools used are a vortex lattice method (VLM) in xflr v6.32, and FEA in ANSYS Mechanical APDL 17.0. Each result from the analysis is compared to theory and convergence checks are performed in line with the method proposed by [3]. To determine locations of interest, or critical failure points, for detailed numerical analysis, a fault tree was developed.

## 4.1 Fault Tree

The following fault tree is for a general UAV flight failure. By determining the failure modes of the UAV, detail design can be focused on the critical failure points identified.

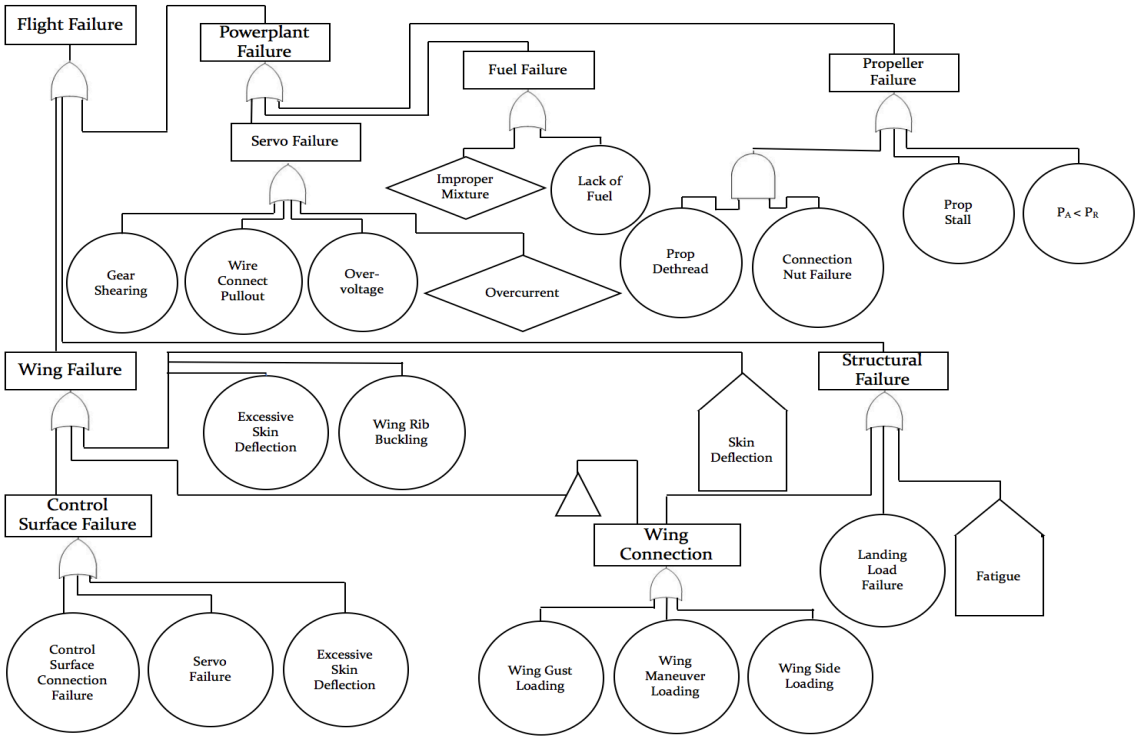


Figure 30. Simplified project vehicle fault tree

The main modes of failure from level flight are the fuselage, powerplant, and wing. In particular, the main structural failures of concern are the wing connection to the fuselage in limit loading from either maneuvering or gust, and the impulse loading from landing. Both failure modes are candidates for finite element analysis. Wing failure loadings are mainly due to the load factors considered in 14 CFR Part 23 (Appendix B). These failures are analyzed in more detail in this section.

## 4.2 Final Design Weight Buildup

The flight forces on the vehicle and flight performance estimates are strongly dependent on the full-fuel and empty weight of the vehicle. A summary of the weight buildup is enumerated in Table 7.

Table 7. Design weight buildup

| Subsystem | Weight | No. | Subsystem Weight |
|---|---|---|---|
| Structure | | | 20.02 oz |
| Wing Skin | 7.6 oz | 2 | |
| Wing Formers | 2.1 oz | 2 | |
| Wing Stringers | 0.012 oz | 10 | |
| Fuselage Frame | 1.2 oz | 1 | |
| Fuselage Skin | 1.4 oz | 1 | |
| Powerplant | | | 20.80 oz |
| OS 35AX Engine | 12.8 oz | 1 | |
| Fuel (Potential) | 8.0 oz | 1 | |
| Electronics | | | 2.020 oz |
| Wing Servos | 0.44 oz | 4 | |
| Powerplant Servo | 0.26 oz | 1 | |

The total system full-fuel weight is approximately 2.59 lb, corresponding to a payload fraction of 0.66. This weight will be used in Chapter 4 for finite element analysis flight force determination, and in Chapter 5 for performance estimation.

## 4.3 Detailed Flight Mechanics

The following section refines the analysis in Section 3.1.2 to include contributions from the propeller (powered stability and trim). The eigenvalues for stability (Equation 22, Chapter 5) are also plotted in this section to determine the general dynamic response to gusts in level flight.

### 4.3.1 Powered Stability and Trim

The total wing moments in this analysis include thrust as a function of velocity T(v), as well as the propeller normal force as a function of velocity $N_p(v)$. Taking Equation 4, dimensionalizing it, and expanding for both alpha and delta derivatives, the equation gives

$$\sum M = \frac{1}{2}\rho u S\bar{c}\left[C_{m_\alpha}(\alpha-\alpha_0)+C_{m_\delta}\delta\right]+\frac{1}{2}\rho u S x_w\left[\left(C_{L_\alpha}(\alpha-\alpha_0)+C_{L_\delta}\delta\right)\cos\alpha - C_{D_\alpha}\sin\alpha\right]+\frac{1}{2}\rho u S z_w\left[\left(C_{L_\alpha}(\alpha-\alpha_0)+C_{L_\delta}\delta\right)\sin\alpha + C_{D_\alpha}\cos\alpha\right]+z_pT+x_pN_p \quad (4.5)$$

The thrust and normal components of the equation can be determined by propeller blade theory (Appendix C). The data from these results are combined to produce the elevon deflection curve seen in Figure 31.

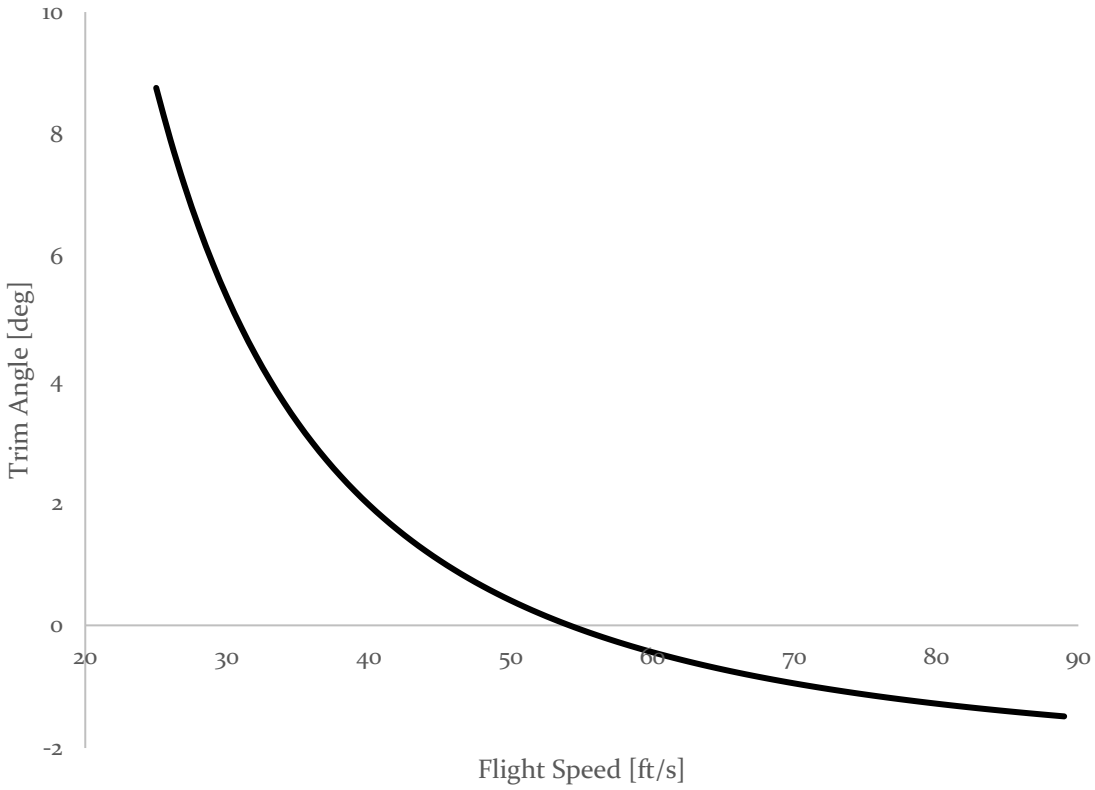


Figure 31. Elevon deflection required for trim as a function of level flight speed

The elevon deflection required to trim the plane at cruise ($v_C$) is approximately 0.5 degrees. This corresponds to a negligible increase drag of less than 0.1 lbf on the system.

Future development could potentially include payloads on the wings of the vehicle. As such, it is imperative to determine the maximum difference in weight allowable between the two wings. Referring to the $C_{L_\alpha}$ curve in Figure 18 (0.05 $deg^{-1}$), and assuming the lift acts at the aerodynamic center of the control surface, the maximum weight differential at the middle of the inner wing payload bay can be

shown to be more than the maximum takeoff weight of the vehicle at all flight speeds. Therefore, this is not of concern in the final design.

### 4.3.2 Dynamic Stability and Response to Perturbations

Linearized dynamic stability equations from Reference [5] are solved for using the process outlines in Section 5.3.3. The vehicle has only one unstable pole in the spiral mode – common in low Reynolds applications. This can be corrected for using a stability augmentation system (SAS) or a large time to double. Either method allows the vehicle sufficient time to correct the response before the path change is too great to correct.

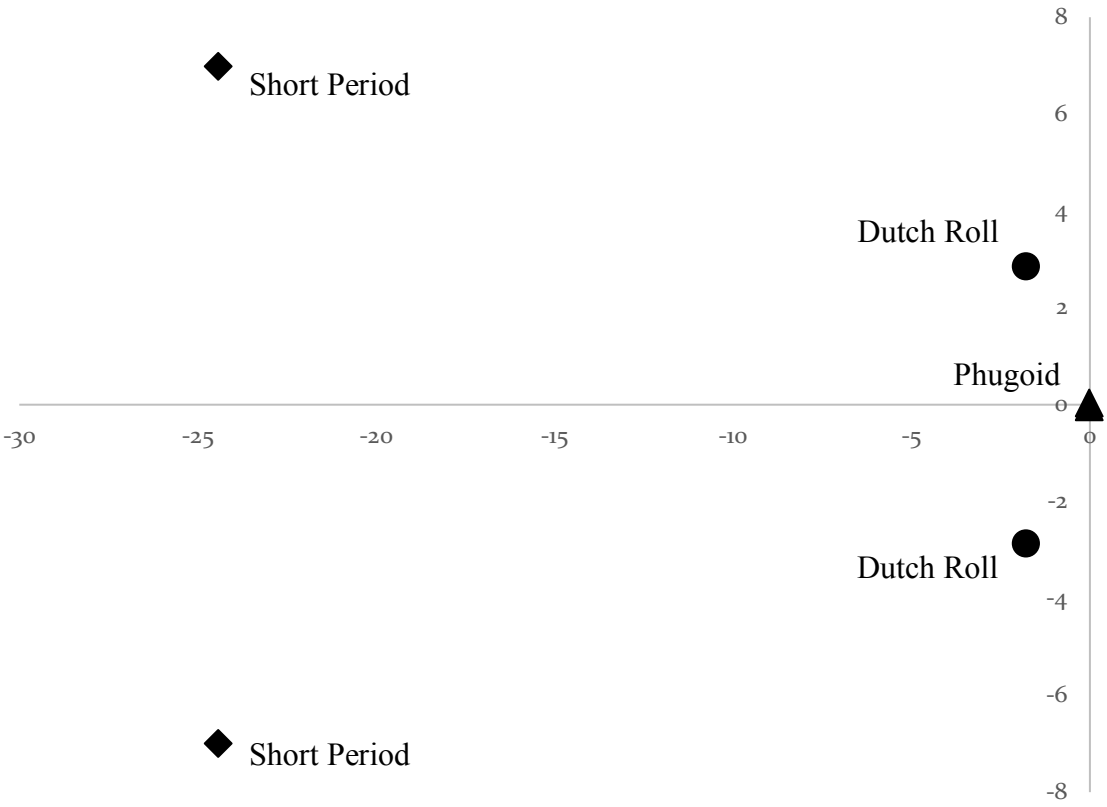


Figure 32. Root locus plot for underdamped modes

All eigenvalues determined in this section (Table 8) are used in Chapter 5 to determine the UAV velocity and position response to flight perturbations.

Table 8. Eigenvalues of dynamic stability modes

| **Mode** | **Eigenvalue [airsec]** |
|---|---|
| Short Period | $-25.12 \pm 45.22j$ |
| Phugoid | $-0.0333 \pm 0.2633j$ |
| Roll | -565.4 |
| Dutch Roll | $-1.781 \pm 17.96j$ |
| Spiral | 0.0088 |

## 4.4 Detailed Structural Analysis

The structural analysis in this section focuses on two main failure modes: wing skin deflection failure, and fuselage failure. The structure of this section goes from most likely to occur failure mode to least likely.

### 4.4.2 Fuselage Finite Element Analysis

All analysis of the fuselage frame uses quasi-isotropic carbon fiber material properties from [16], and readily available, inexpensive, unidirectional carbon fiber tubes from [17]. The fuselage, in each case, is simplified to only include the main stressed component and is fixed at the top to simulate the maximum potential stresses that could occur within the frame itself.

The landing loading in this analysis is simplified by using D'Alambert's principal to find an equivalent static load factor of 2.6 (Appendix B). This is applied to the locations specified in Figure 24. The top surface of the fuselage frame is fixed to simulate the maximum compressive stresses possible in the bottom linkages of the frame.

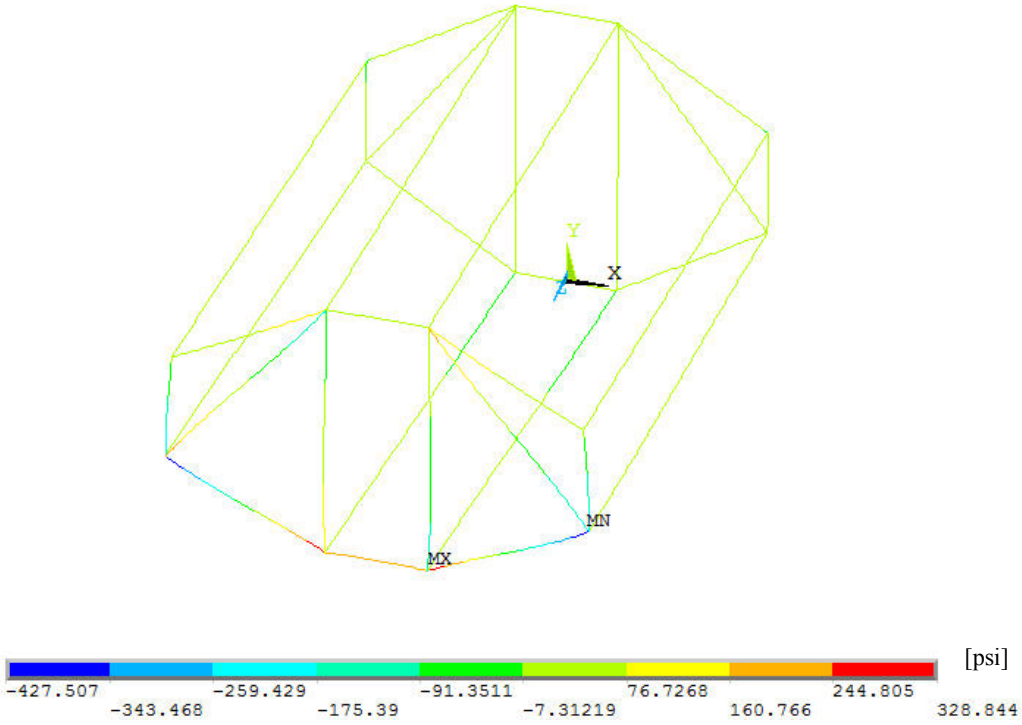


Figure 33. Converged FEA results for landing loading on frame

The landing loading yields a maximum stress at the point of application, corresponding to the maximum bending load in the frame at that point (MX). The minimum stress in this loading corresponds to the maximum compressive stresses on the frame. This occurs at the underside of the wing connection point (MN). Maximum principal stress theory is used as the failure criterion for this analysis. Tsai-Wu failure theory is not required, because of the high factors of safety inherent in the use of composite materials for this application. The maximum principal stresses for various element sizes is shown in Table 9.

Table 9. Landing load maximum principal stress convergence table

| Element Size [in] | Stress [psi] |
|---|---|
| 0.2500 | 303.9 |
| 0.1250 | 320.5 |
| 0.0625 | 328.8 |

Using [2] to estimate the error in the analysis, the error is estimated to be 2.56%. This is well within the acceptable limits suggested by Sinclair.

Maneuvering loading, or the increased lift associated with bank angle, must also be analyzed. The maneuvering loading required for this UAV is determined by 14 CFR 23.333, and is, for a normal class plane, +3.8. This loading is applied to the wing connection points, while the bottom of the fuselage is fixed to simulate a worst-case lift loading (similar to Figure 22). A contour plot of the resultant stresses is shown in Figure 34.

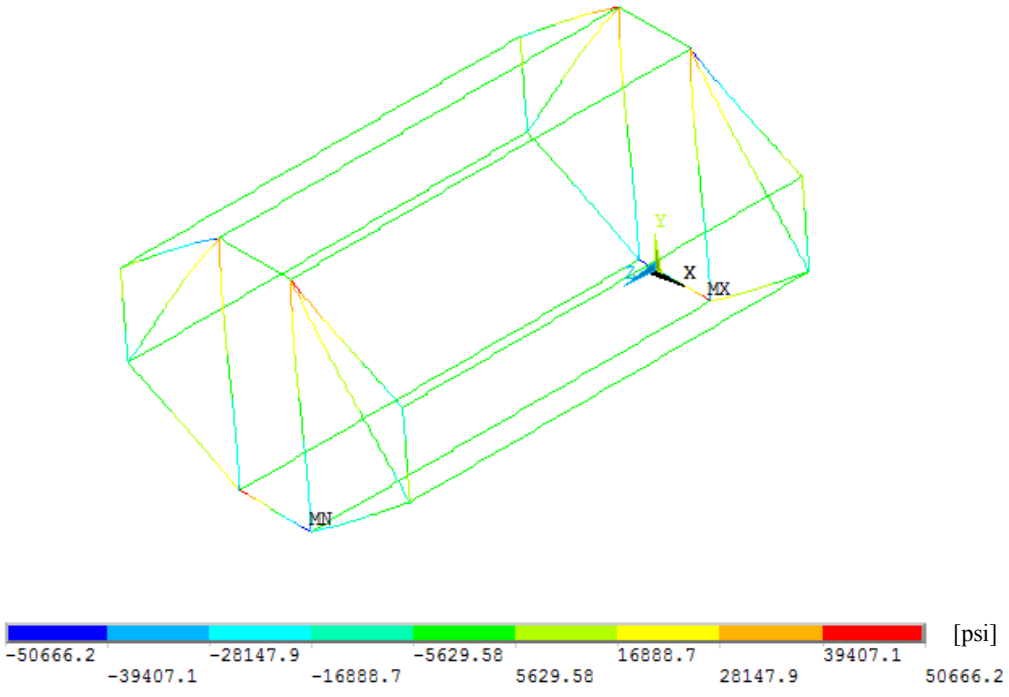


Figure 34. Wing maneuvering loading

The converged stresses for this loading are enumerated in Table 10.

Table 10. Maneuvering loading maximum principal stress convergence table

| Element Size [in] | Stress [psi] |
|---|---|
| 0.2500 | 49500 |
| 0.1250 | 50300 |
| 0.0625 | 50700 |

It should be noted that the converged maximum stress of 50.7 ksi corresponds to a factor of safety of more than 1.5 in the fuselage frame. Therefore, the ultimate loading factor of safety, as defined by 14 CFR §23.303 is met. The stress maximum and minimum are the same from this analysis corresponding to pure bending in the member. The UAV in question, then, meet all standards required for two of the main failure modes of a UAV.

### 4.4.1 Wing Skin Deflection

The initial elevon deflection to trim is found by determining the change in total UAV lift and moment coefficients required for different flight regimes, as shown in Section 4.3.1. However, if the wing skin deflects significantly in reasonably expected flight conditions, the airfoil shape will not be maintained, and the elevon will have sufficient control authority to maintain level flight (greater than 5 degree control surface deflection, as defined in Chapter 3). Therefore, the deflection of the skin should be analyzed.

The deflection on the wing skin is dependent on the pressure distribution along the wing, and the direction of the fibers. 3D vortex panel methods in xflr v. 6.32 were used to determine this distribution in both the span-wise and chord-wise direction, and orthotropic approximations of the anisotropic properties from

Reference [16] were used to model the behavior of the wing skin in flight. Figures 35 and 36 show a converged skin deflection solution, it can be seen that the maximum skin deflection occurs at the middle of the wing elevon section. The difference in deflection of the wing skin is less than 1/32 inch at this location.

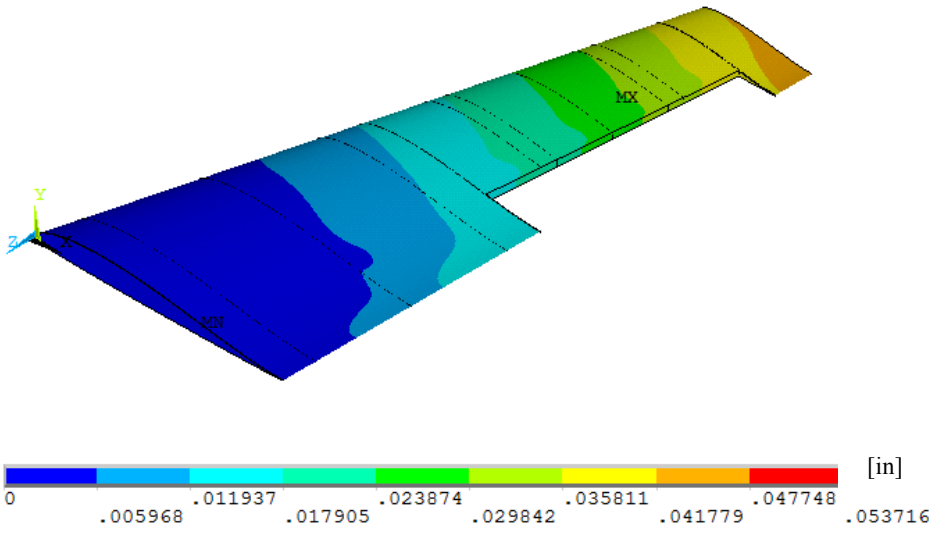


Figure 35. Isometric view of wing skin deflection

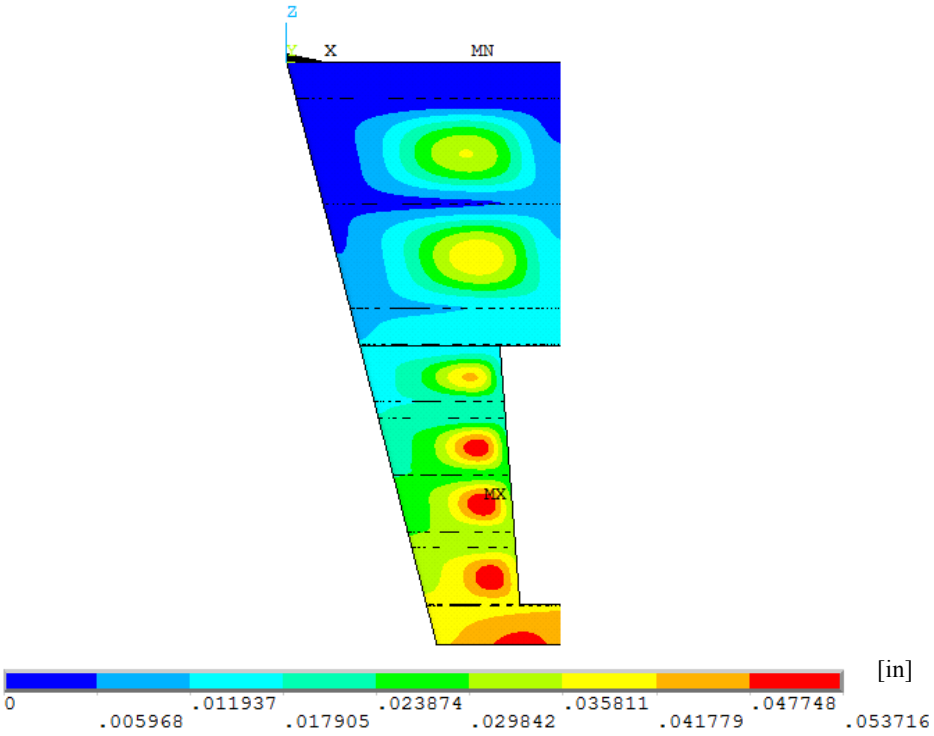


Figure 36. Bottom view of wing skin deflection

Using the lift-modified airfoil in xflr v. 6.32, and using VLM, the performance change due to skin deflection was analyzed. The total change in lift for the plane, and the total change in moment of the plane were each less than 1%. Therefore, the skin deflection is neglected in future analysis.

## 4.5 Final Design Overview

The final Project UAS has a total reduction in zero-lift wing drag from the initial conceptual design of 214%, from 0.033 to 0.0105. The addition of winglets reduced the drag by an additional 15%, as well as increased the directional stability derivative ($C_{N_\beta}$) from less than $10^{-5}$ to over $5 \times 10^{-3}$ $deg^{-1}$, allowing the UAS to properly handle side loading. This allows the UAV to maneuver without the addition of a stability augmentation system.

The dynamic response of the UAS allows a change in CG location to be greater than the required 7% travel. This will allow the planform to be highly modular, allowing the end user to customize the design experience. The dynamic modes meet all requirements for stability, except the spiral mode. This is corrected by the large response time of the plane. The potential addition of a stability augmentation system will allow the plane to damp these responses, and will allow for the UAV to further increase the directional and lateral static stability of the plane.

Due to the low zero-lift drag and low trim drag on the planform, the plane endurance exceeds the Client specified three hours. Potential design modules can increase the UAS flight time to over 24 hours of total flight time, while still maintaining the requirement to be launched by hand. It is determined, therefore, that the design requirements of all stakeholders in the design are met.

# Chapter 5. Final Iteration Performance Estimation

The following chapter outlines basic performance analysis for the final design iteration. It combines closed form solutions from references [5] and [6], as well as derived equations for linearized perturbation velocity estimation. The analysis will follow a typical flight from takeoff and climb, to level flight, and concluding in sink and landing.

## 5.1 Takeoff

Takeoff analysis can be performed using the formula $\vec{v}d\vec{v} = \vec{a}d\vec{s}$, where $\vec{v}$ is the velocity vector of the plane, $\vec{a} = \frac{g}{W}\vec{F}$, $\vec{F}$ is the total flight force on the vehicle, and $\vec{s}$ is the CG displacement vector.

For this analysis, the forces on the vehicle are assumed to be simply body-centered lift, drag, thrust, weight, and a 5% male pull force to approximate the minimum likely launch force [11]. The following semi-empirical relation can be derived:

$$\frac{W}{g}\frac{\vec{v}}{F_{launch}+\vec{T}(\vec{v})-\vec{D}(\vec{v})}d\vec{v} = d\vec{s} \qquad (19.1)$$

Integration of equation 19.1, yields

$$\frac{W}{g}\int_0^v \frac{\vec{v}}{F_{launch}+\vec{T}(\vec{v})-\vec{D}(\vec{v})}d\vec{v} = \int_0^{\pi r/2} d\vec{s} \qquad (19.2)$$

where r is the location from the center of rotation to the center of gravity of the plane. The results of Equation 19.2 are shown in Figure 37 for the Project vehicle.

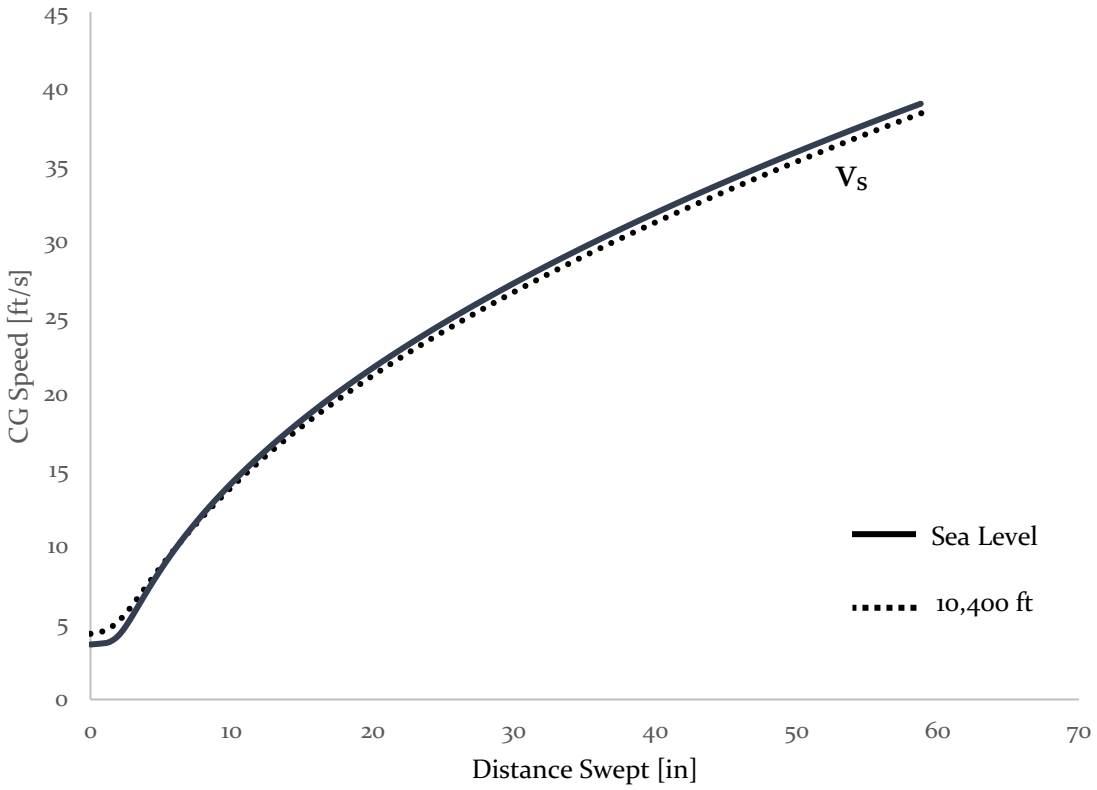


Figure 37. CG speed with respect to the distance travelled in hand-launch

At both sea level, and 10,400 ft, the final velocity is 32 ft/s, above the stall speed ($v_S$). Therefore, it is concluded that the plane is able to be launched by hand by a 5% male, meaning the majority of users should be able to launch the vehicle by hand. After takeoff velocity is achieved, a climb analysis will determine the vehicle's ability to complete the takeoff maneuver at sea level and 10,400 ft.

## 5.2 Climb

Assuming small angles between the thrust vector and the fuselage longitudinal axis, the climb speed (the vertical component of speed) can be calculated from [6] as

$$v_z = \frac{P_A - P_R}{W} \qquad (20)$$

where $v_z$ is the vertical component of speed, $P_A$ is the available power, shown earlier, and $P_R$ is the power required to overcome drag. The results for sea level and 10,400 ft can be seen in Figure 38.

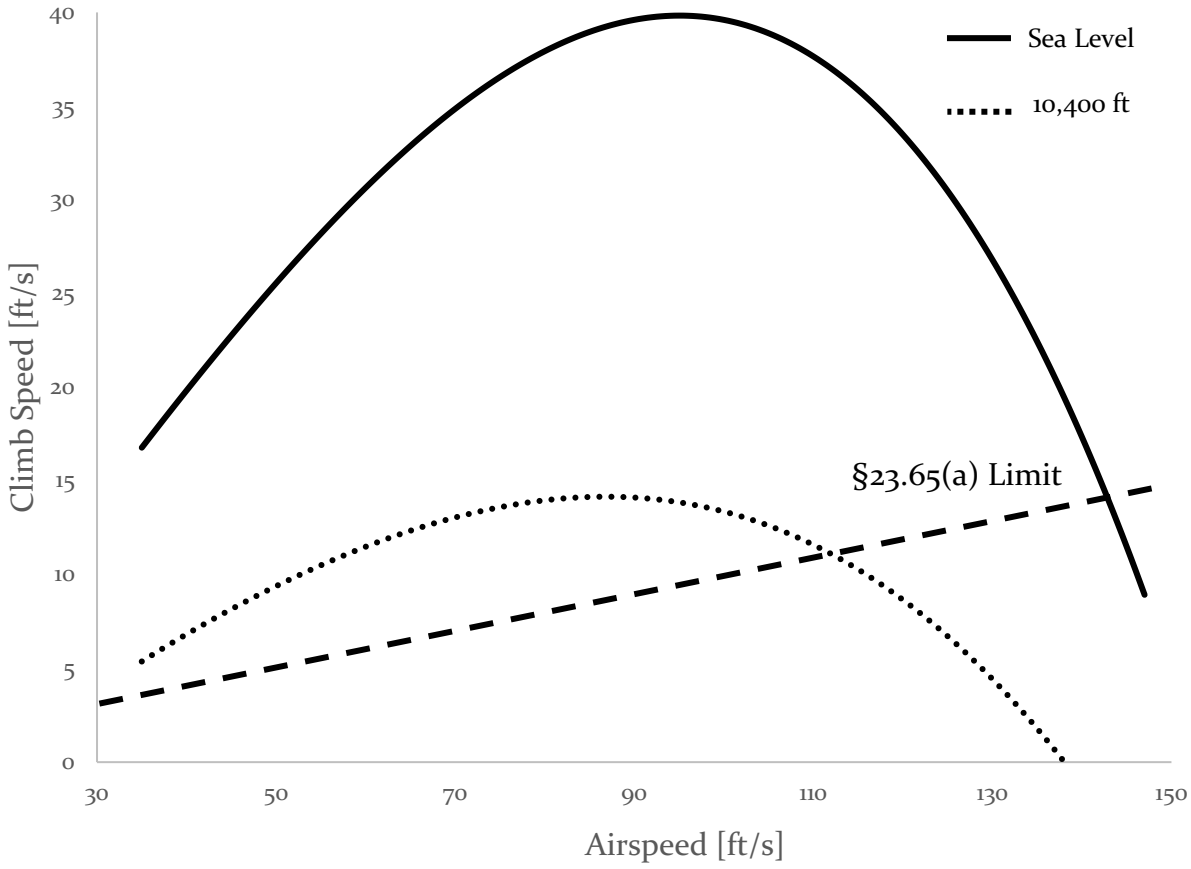


Figure 38. Wide open throttle vertical climb speed

The climb speed must be at least, as per 14 CFR Part §23.65(a) 8.3% of the ground speed. The vehicle, then, is capable of maintaining steady climb up to 115 ft/s at sea level, and 142 ft/s at 10,400 ft.

For this design, the service ceiling should exceed 10,400 ft. to ensure that the end user can operate the UAV in all potential flight regimes. The service ceiling for an aircraft is defined as the density altitude where the maximum vertical component

of the velocity is less than 100 ft/min under max throttle conditions. The absolute ceiling is where the plane can no longer climb, or where the maximum vertical component of the velocity goes to zero. The service ceiling for this UAV is calculated through iteration as 12,000 ft., and the absolute ceiling is 12,500 ft.

## 5.3 Level Flight

Level flight is split in this thesis into two main topics: maneuvering, and response to perturbations. The structure of this section will also follow a typical level flight path from maneuvering to level flight. To ensure that the vehicle can turn under constant speed conditions, the maneuvering radius with respect to speed is determined. The endurance and range of the vehicle calculated in Chapter 3 will also be refined using analytical solutions from [6]. Finally, the vehicle response to gusts, or perturbations, will be estimated.

### 5.3.1 Maneuvering

A steady, level turn requires that the speed of the vehicle be maintained and no bank angle ($\gamma$) present shown in Figure 39.

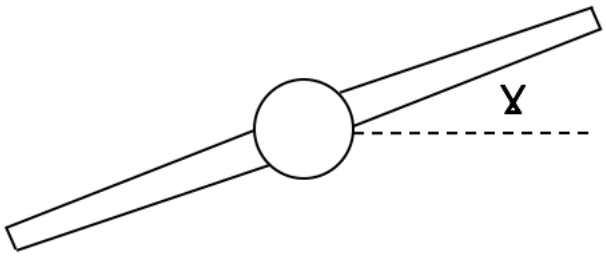


Figure 39. Steady, level turn bank angle

Using a combination of the limiting turn radius

$$R = \frac{v^2}{g\sqrt{n^2-1}} \qquad (21)$$

and the definition of the load case (Equations 11.1 & 11.2), the stall-limited turn radius can be determined. The structure limited turn radius is determined using the maneuvering load factor of +3.8 from Appendix B, and Equation 19.

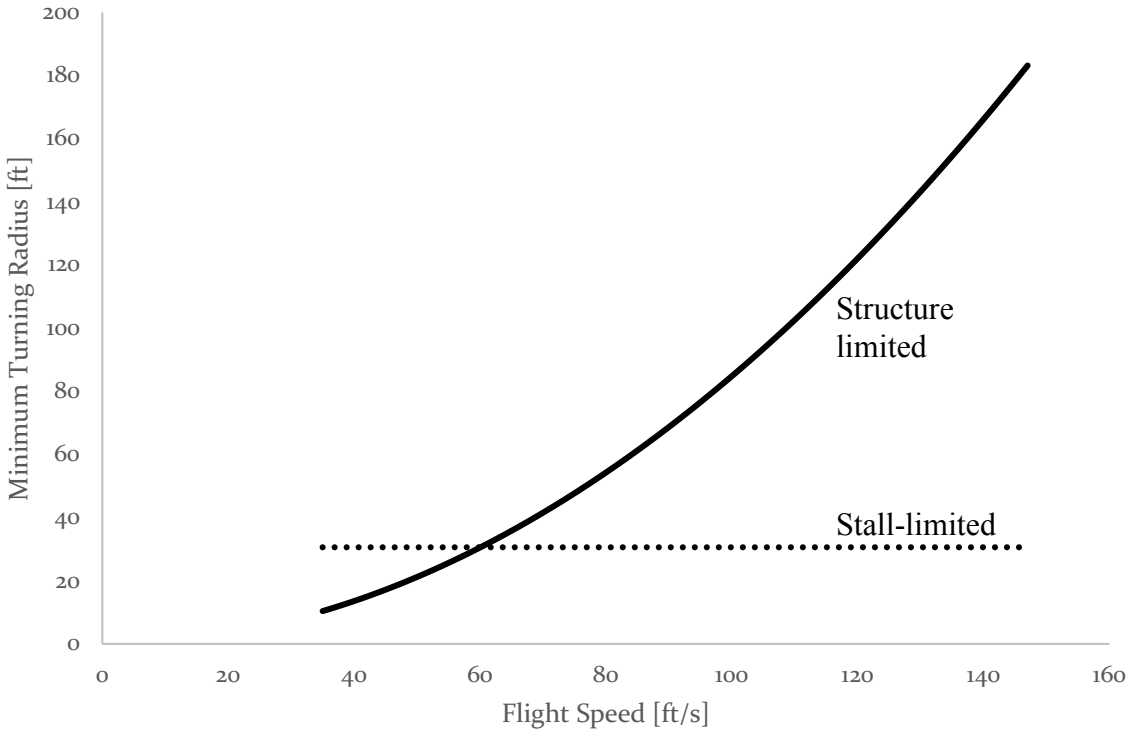


Figure 40. Minimum turning radius of vehicle for two limiting cases

The larger value in Figure 40 refers to the larger radius, or the limiting case. Until 60 ft/s, the stall limited turn radius of 30.6 ft is the minimum turn radius. After this point, the turn is limited by Part 23 load factors.

### 5.3.2 Endurance and Range

After the takeoff and typical maneuvering phases, the level flight endurance and range determine the flight time of the vehicle. The minimum required endurance is 3 hours (Table 2), and the minimum range is approximately 200 miles (Appendix A). All calculations in this section assume a total engine efficiency of 30%, and the chemical potential energy in a full gasoline fuel.

No headwind endurance is defined as the total flight time of the plane if there is no component of velocity induced by wind. The no-headwind maximum endurance can be easily calculated for a propeller as

$$E_{max} = \frac{2(3\pi eA)^{3/4}}{\sqrt{32}C_{Do}{}^{1/4}} \frac{\sqrt{\rho S}}{q_P} \left( \frac{1}{\sqrt{w_e}} - \frac{1}{\sqrt{W_f}} \right) \qquad (21)\ [6]$$

where $q_P$ is the specific fuel consumption, $W_e$ is the weight of the plane with all useable fuel spent, and $W_f$ is the maximum takeoff weight of the plane for the specific flight conditions. For sea level, half a pound of fuel yields approximately 30 hours of flight time, and for 10,400 ft., half a pound of fuel yields approximately 24 hours of flight time. This is comparable to high-end fixed wing UAS seen in Appendix A.

The no headwind case for maximum range is calculated in a similar manner to the no headwind endurance. This analysis assumed the vehicle is flying at the minimum drag speed [6]. For a propeller-driven aircraft, the range can be estimated by

$$R_{max} = \sqrt{\frac{\pi eA}{4C_{Do}}} \frac{1}{q_P} \ln \left( \frac{W_f}{W_e} \right) \qquad (22)\ [6]$$

For sea-level, the maximum range for half a pound of fuel is 950 miles, and for 10,400 ft. the maximum range is approximately 700 miles.

### 5.3.3 Perturbation Response

The analysis in this subsection is performed only at sea-level to model the most likely flight conditions of the Project UAS. The response to perturbations in this thesis are split into three main underdamped modes: short period, and phugoid modes as longitudinal responses; and Dutch Roll as a combined directional and lateral response. The longitudinal case is explained in detail to demonstrate the process used in analysis. The non-dimensional longitudinal stability tensor equation is defined as

$$\begin{bmatrix} 2\mu - C_{x_u} & C_{x_\alpha} & C_{L_o} \\ 2C_{L_o} - C_{z_u} & 2\mu - C_{z_{\dot{\alpha}}} & 2\mu + C_{z_q} \\ C_{m_u} & C_{m_\alpha} + C_{m_{\dot{\alpha}}} & i_B - C_{m_q} \end{bmatrix} \begin{bmatrix} \hat{u}_o \\ \alpha_o \\ \theta_o \end{bmatrix} = 0 \qquad (23)\ [5]$$

where u derivatives are derivatives with respect to speed, “α” derivatives are with respect to angle of attack, “$\dot{\alpha}$" are with respect to the time rate of change in the angle of attack, and “q” derivatives are with respect to the pitch rate [5]. This is calculated in this thesis using xflr v6.32. The position of the plane in the x-z, or longitudinal plane, is determined by integrating the velocity response through the relation

$$\vec{x} = \int_0^t \vec{v}\, dt \qquad (24)$$

where $\vec{x}$=*f* (x,z), and v=*f* (x,z). The Dutch Roll response is similar in process, except it uses the velocities in the directional plane to calculate the UAV position with respect to time.

Table 11. Full fuel underdamped dynamic stability responses

| Mode | Eigenvalue [airsec] | TTH [airsec] | T [airsec] | $N_{half}$ |
|---|---|---|---|---|
| Short Period | $-25.12 \pm 45.22j$ | 0.0275 | 0.139 | 0.198 |
| Phugoid | $-0.0333 \pm 0.2633j$ | 20.7 | 23.9 | 0.867 |
| Dutch Roll | $-1.781 \pm 17.96j$ | 0.387 | 0.350 | 1.11 |

Table 12. No fuel underdamped dynamic stability responses

| Mode | Eigenvalue | TTH [airsec] | T [airsec] | $N_{half}$ |
|---|---|---|---|---|
| Short Period | $-30.49 \pm 54.25j$ | 0.0226 | 0.116 | 0.195 |
| Phugoid | $-0.0374 \pm 0.2461j$ | 18.5 | 25.5 | 0.724 |
| Dutch Roll | $-2.092 \pm 20.41j$ | 0.330 | 0.308 | 1.07 |

The eigenvalues for underdamped responses are written by convention as $\lambda = n \pm \omega j$ where $\lambda$ is the eigenvalue, n is the real part of the response, and $\omega$ is the imaginary part of the response. The real part of any perturbation response corresponds to the plane time to half, or time to double (the time it takes for the perturbation amplitude to double or half). The imaginary part corresponds to the plane damping ratio and period response, often reported in airseconds. This is a non-dimensional time defined by Etkin as $t/t^*$ where $t^* = \frac{l}{u_o}$ where $u_o$ is the original plane flight speed, and $l$ is half of the plane MAC in longitudinal equations and half of the plane span in lateral equations [5].

The time to half in the tables is calculated from Etkin as $t_{half} = \frac{0.69}{|n|}$. The tables include the period of the perturbation oscillation in airseconds, as well as the number of cycles to half ($N_{half}$). The perturbation period is defined in Etkin as $T = \frac{2\pi}{\omega}$ and the cycles to half are defined as $N_{half} = \frac{t_{half}}{T}$. From the data presented in Tables 11 and 12, it can be seen that the plane response to perturbations becomes more stable with a decrease in the fuel weight. The amplitude of perturbations, however, increases as well. This is attributed to the decrease in total plane weight.

The UAV short period response corresponds to a large change in plane Euler angle in the x-z plane, and a small change in the plane velocity [5]. The velocities of concern in the short period mode are the x velocity (u) and z velocity (w). From the curve presented in Figure 41, it can be seen that the UAV returns to the initial flight speed in less than ¼ second. Though the flight speed values are high, the time that the plane is subjected to each is exceedingly small. Therefore, the short period mode is deemed to be heavily damped, as per 14 CFR 23.181(a).

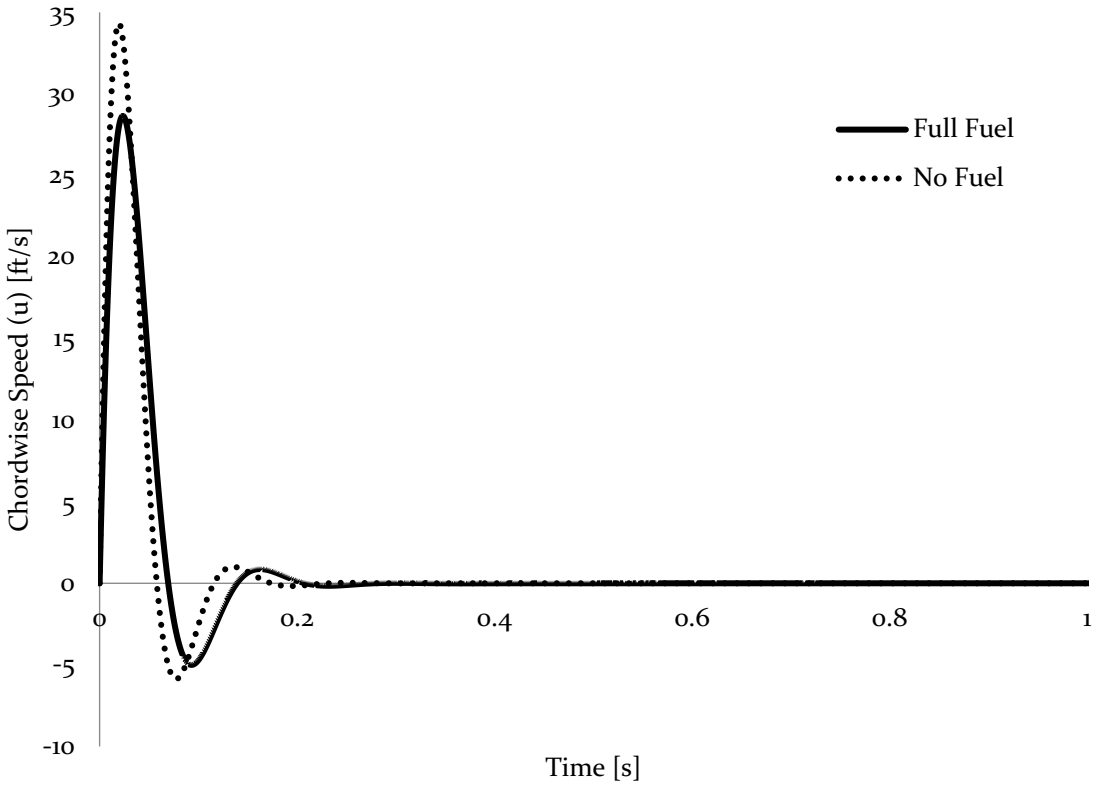


Figure 41. Short period chord-wise velocity response

The typical dynamic response of a phugoid mode corresponds to small changes in plane angle in the x-z plane, and a relatively large change in the flight speed. This corresponds to the less damped longitudinal eigenvalue [5]. The velocity response can be seen in Figure 42.

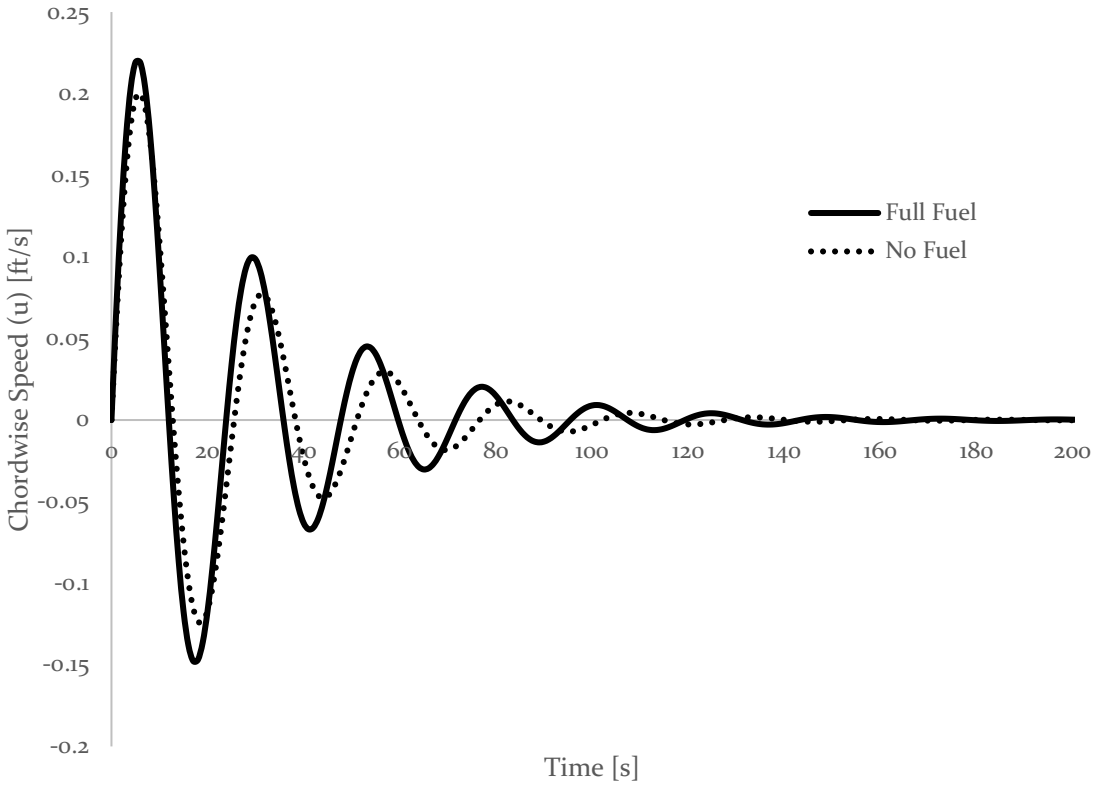


Figure 42. Phugoid chord-wise velocity response

14 CFR 23.173(b)(1) states that the total change in plane forward velocity cannot exceed 10% of the original flight speed. To determine the total change in forward speed, a trapezoid rule numerical integration is applied to the modal response in Figure 42. For both cases, the total final speed change is less than 1 fps.

The Dutch roll is defined in [5] as the combined lateral and directional motion of a plane. Due to the coupling of lateral and directional motions, the Dutch roll is typically the only stability mode in the lateral and directional responses that yields a complex eigenvalue (Tables 11 - 12).

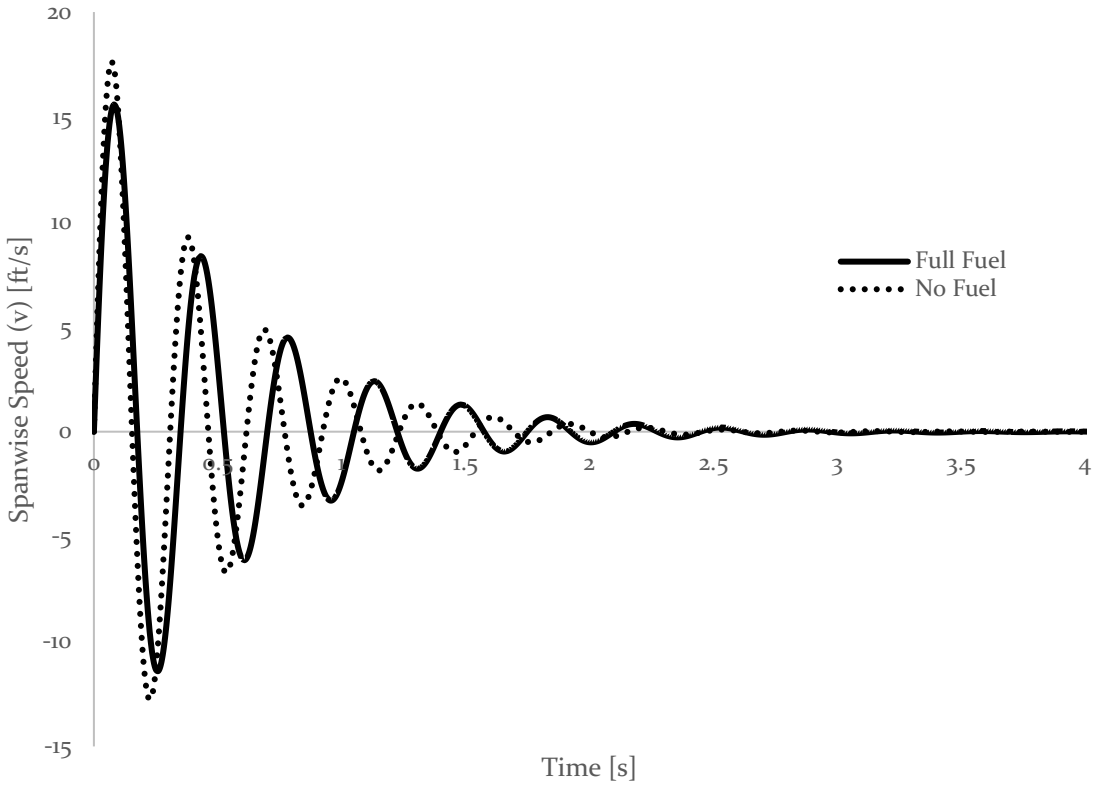


Figure 43. Dutch roll span-wise velocity response

Comparing the amplitude of the Dutch roll spanwise speed, it can be seen that the amplitude of the velocity is more than 1/10 the amplitude of the initial velocity in seven cycles. The vehicle, however, meets this criterion in eight cycles with no damping from control surfaces. With the addition of a stability augmentation system (SAS), as per 23.181(c), and 23.672, the vehicle can damp the perturbation in less than seven cycles by activating the control surfaces. Experienced pilots, as well, can allow for flightworthiness to be tested by manually activating controls.

Referring to Figures 41 and 42 for the vertical component of velocity (w) with time, the position is estimated for the short period mode in Figure 44 and for the phugoid mode in Figure 45.

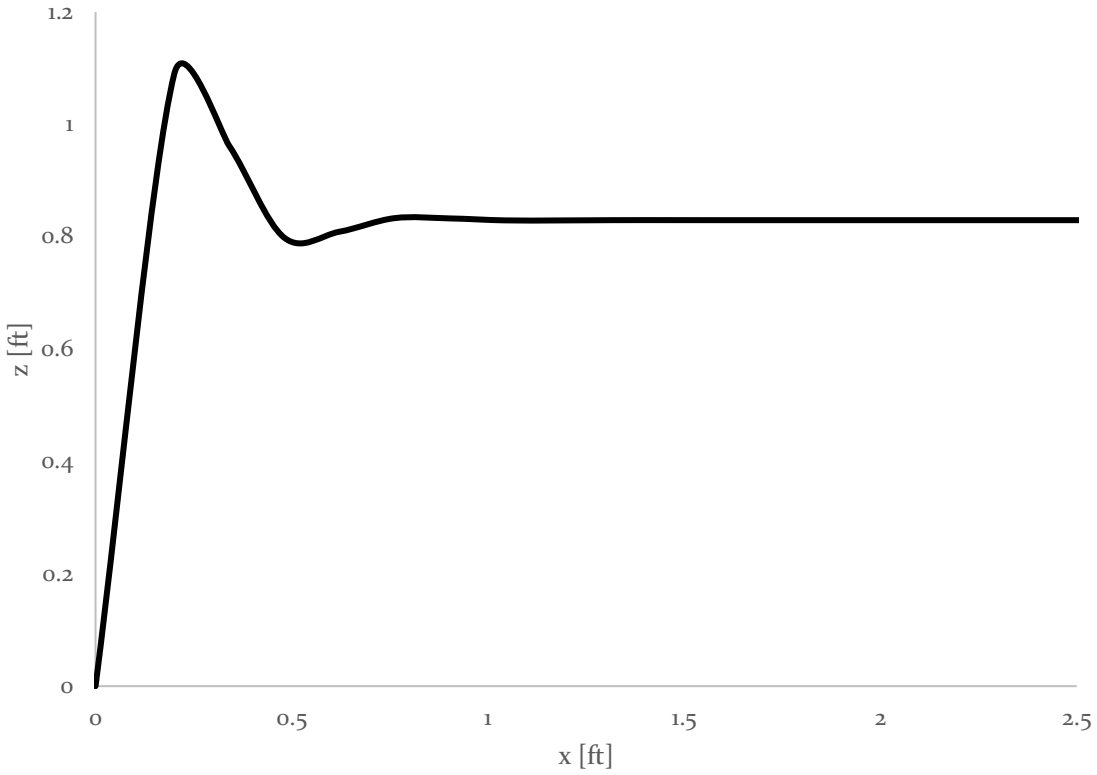


Figure 44. Short period position estimation

The short period mode seen in Figure 44 shows that the UAV levels out within one foot of the original flight path. This is within the margin of error for most inexpensive GPS systems and, as such, it is deemed negligible. The phugoid mode, as previously mentioned does not have large changes in position. The plane, however, does tend to increase speed in the chord-wise direction.

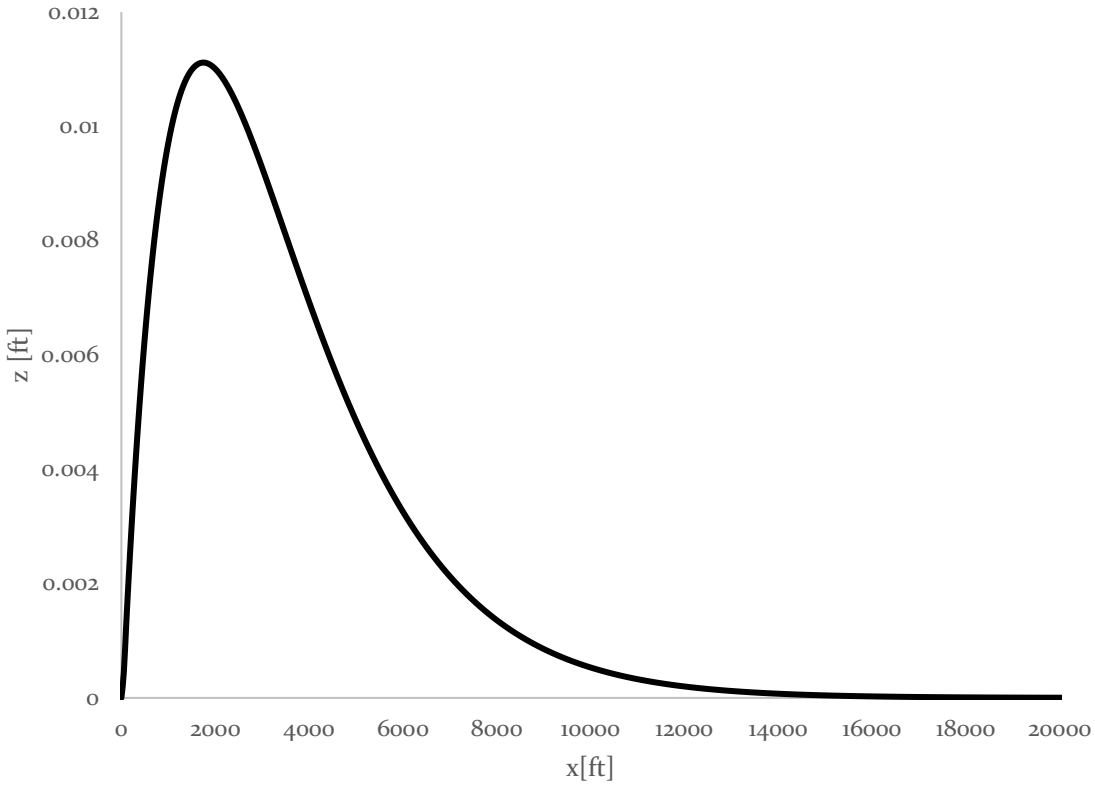


Figure 45. Phugoid mode position response

The maximum displacement of the plane is approximately 0.011 ft – less than the short period mode. This, then, is also acceptable for flightworthiness.

The Dutch roll mode assumes a perturbation in only the directional plane, shown in Figure 46.

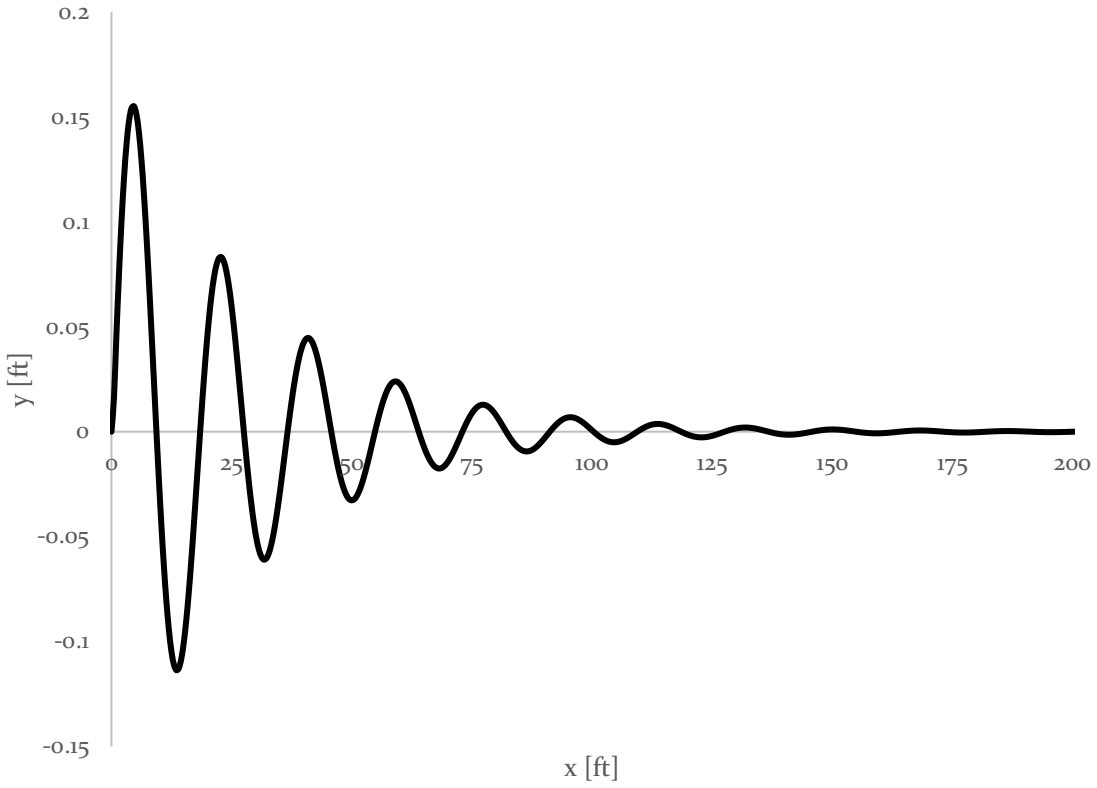


Figure 46. Dutch roll position response

The response to perturbation is, at maximum, 0.15 ft. This is, again, within the margin of error of most readily available GPS units. The design, then, is deemed acceptable.

## 5.4 Landing

The landing distance can be easily found from the same differential equation as takeoff, while assuming that there is no launch force, there is no thrust being produced by a static propeller, and that the rolling resistance on the plane wheels is constant. The equation becomes

$$\frac{W}{g}\frac{\vec{v}}{-F_{\mu}(\vec{v})-\vec{D}(\vec{v})}d\vec{v} = d\vec{s} \qquad (25)$$

where the left-hand side of the equation is integrated from the landing speed, approximately $1.15v_S$, to zero. Assuming a rolling resistance of 0.04, corresponding to a general resistance of rubber on asphalt, the landing distance at sea level can be shown to less than 60 ft.

## 5.5 Performance Review

The UAV designed for this thesis is required to be hand launched by the Client, and, naturally, to be able to withstand the maneuvering loading placed on the frame. Using the closed-form solutions from Phillips and deriving relations from first principles, it can be seen that a typical male can launch the plane by hand by exceeding the stall speed of 32 ft/s. This includes the UAV's ability to climb at altitude. The service ceiling on the plane is over 2000 ft from the highest launch altitude, exceeding the 400 ft maximum altitude set by the FAA.

End users have specified that a high degree of accuracy in surveying is required. Therefore, the response to perturbations is required to be low. From the eigenvalues estimated in xflr v6.32, the velocity and position responses determined. A review of these responses show that the maximum speed differential is less than 2% in the phugoid mode, and the maximum altitude differential is less than 2% in the short period mode. The performance specifications of all stakeholders in the design are met.

# Chapter 6. Conclusion

The initial design requirements of the UAS in this thesis are to be a flightworthy aircraft that has over a 3 hour endurance, and is launched by hand. The market further required that the vehicle be modular in nature, requiring sufficient control authority for static stability over a large change in CG location. The design process consisted of three main phases: conceptual design, preliminary design, and detail design.

An initial design that is able to lift a payload weight of 5 lb, with a structural weight of 5 lb was determined in the conceptual design (Chapter 2). The preliminary design process reduced the drag on the wings, and increased the endurance and range of the vehicle. It also reduced the total plane weight 50%, through the design of a composite frame and skin system.

Finally, in the detailed design phase, the plane position and velocity response to perturbations was determined. All modes of flight except the spiral mode are heavily damped, meaning that the final planform is designed to minimize deviation from the initial flight path. Because of the high stability derivatives, the vehicle is not able to quickly change from a set flight path at high speeds. The addition of a stability augmentation system (SAS) would reduce potential flight difficulties for a pilot, and would be the first step in fully autonomous flight. It is therefore recommended to use a pre-packaged SAS, such as a Pixhawk, on the final product. A simplified view of the vehicle can be seen in Figure 47.

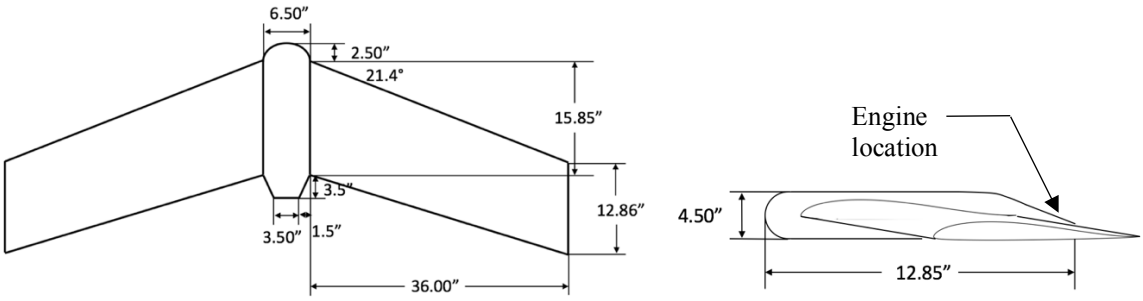


Figure 47. Simplified views of the project UAS

All flight modes of a typical UAS were also analyzed from takeoff to landing. The vehicle response to perturbations was estimated for each of the stable flight modes and compared to 14 CFR Part 23. The longitudinal responses to motion are stable, and meet these requirements; the Dutch Roll response is one cycle outside of FAA requirements with just body damping. However, the SAS will be able to activate all needed control surfaces and meet flightworthiness standards. The cost of the materials of the vehicle are estimated to be under $1800 including a SAS, allowing for a feasible market price of $10,000. A table of the met design parameters are seen in Table 13.

Table 13. Design parameters met and summary of the vehicle parameters

| | |
|---|---|
| Cruise Speed | 60 ft/s |
| Max Speed | 120 ft/s |
| $C_{L_{max}}$ | 1.4 |
| MTOW | 10 lb. |
| CG Travel | ±8% |
| Endurance | 3 hours |
| Range | 200 mi |

# References


1. Code of Federal Regulations § 23 (2013). Print

2. Code of Federal Regulations § 107 (2016). Print

3. Sinclair, G. B., J. R. Beisheim, and S. Sezer. Practical Convergence-Divergence Checks for Stresses from FEA. Proc. of International ANSYS Conference. N.p.: ANSYS, 2006. Web.

4. Roskam, Jan. Airplane Design Part II: Preliminary Configuration Design and Integration of the Propulsion System. Lawrence, KS: DARcorporation, 2004. Print.

5. Etkin, Bernard, and Lloyd Duff. Reid. Dynamics of Flight: Stability and Control. New York: J. Wiley & Sons, 1996. Print.

6. Phillips, Warren F. Mechanics of Flight. Hoboken: John Wiley & Sons, 2010. Print.

7. Nita, M., and D. Scholz. Estimating the Oswald Efficiency Factor from Basic Aircraft Geometrical Parameters. Proc. of Deutscher Luft- Und Raumfahrtkongress. N.p.: n.p., 2012. Print.

8. "Energy in Natural Processes and Human Consumption - Some Numbers." University of Washington School of Oceanography, 2005. Web.

9. "Talon Series: Fixed Wing Unmanned Aircraft Systems." UAV Solutions, 2016. Web.

10. "Lynx UAS." Swift Radioplanes, 2016. Web.

11. Human Engineering Design Data Digest (2000): n. pag. Web.

12. Diederich, Franklin W. "A Simple Approximate Method for Obtaining Spanwise Lift Distributions Over Swept Wings." National Advisory Committee for Aeronautics (1948): n. pag. Web.

13. STI Group - Industrial, Midstream & Fabrication Services. "The Louisiana Oil and Gas Industry Growth: Refineries & Petrochemical Plants." STI Group - Industrial, Midstream & Fabrication Services, 22 Sept. 2014. Web.

14. 3DR. "Solo Specs: Just the Facts." 3DR News. 3DR News, 04 May 2015. Web.

15. “WHAT IS INCLUDED WITH THE COMPLETE READY TO FLY EAGLE XF PACKAGE?" UAV America. N.p., n.d. Web.
b.

16. "Mechanical Properties of Carbon Fibre Composite Materials, Fibre / Epoxy Resin (120°C Cure)." Performance Composites, n.d. Web.

17. “Tube – Pultruded Unidirectional – 0.188 x 0.079 x 78 Inch.” RockWest Composites, n.d. Web.

18. Drela, Mark, and Youngren, Harold. “xfoil 6.9 User Primer.” Massachusetts Institute of Technology Department of Aeronautics and Astronautics (2001). Web.

19. Owens, A., Jarmulowicz, M., and Jones, P., "Structural Considerations of a Baja SAE Frame," SAE Technical Paper 2006-01-3626, 2006, doi:10.4271/2006-01-3626.

20. “Lightweight Carbon Fiber Fabric.” CST Sales, 2016. Web.

21. “35AX.” O.S. Engines, 2017. Web.

22. “APC Performance Data Files.” APC, n.d. Web.

23. King, Sean, and John King. Feb. 2017.

# Appendix A. Market Survey and Differentiation

The project design requires that the market be able to bear the cost and maintenance of the UAS. Therefore, a survey issued to potential end users determined the market price of the platform, approximately $10,000. The following appendix lists the competition for the Project UAS, and potential modules.

## A.1 Review of Market Competition

A general plot of the estimated max speeds and power consumptions can be seen in Figure 48.

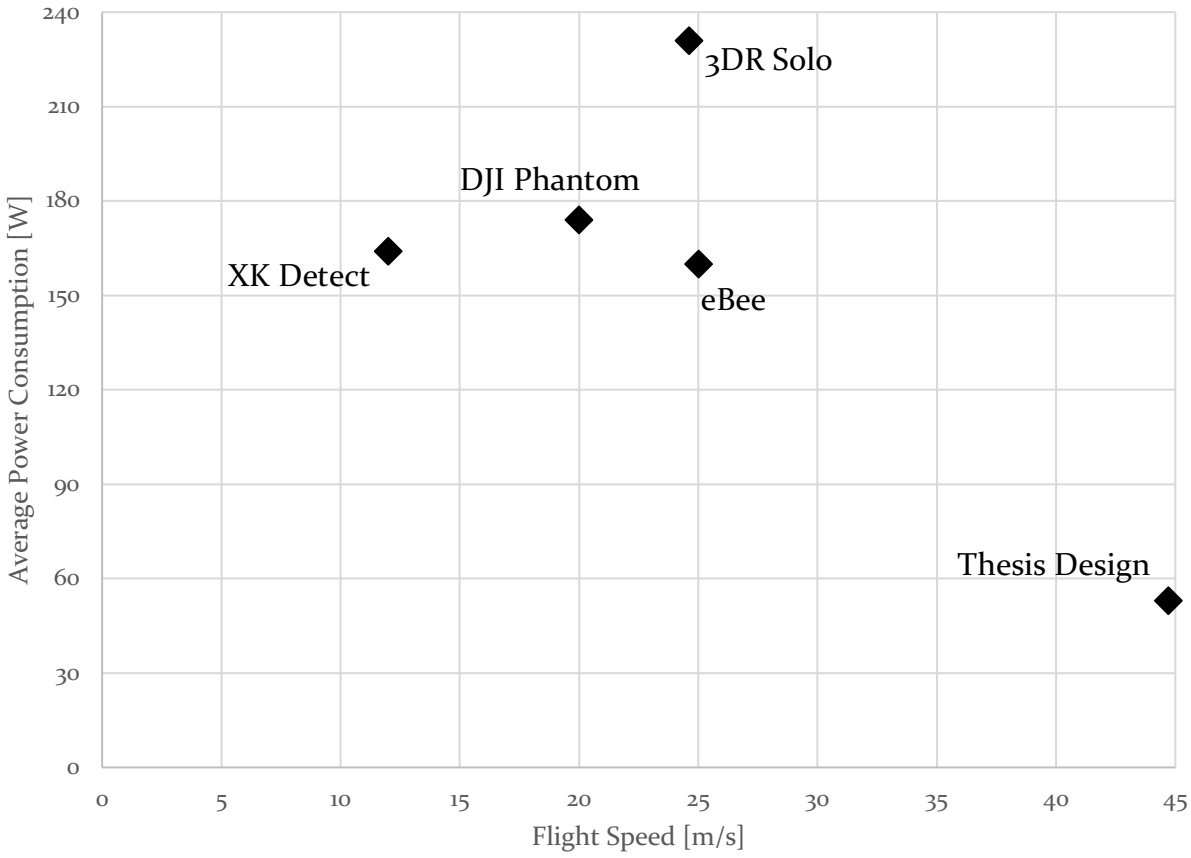


Figure 48. Power consumption and max speed of various UAS

The more efficient the flight, the closer the point will be to the bottom right corner. It becomes obvious, then, that fixed wing craft tend to have better efficiency, and thus a longer flight time. It can also be seen, then, that the proposed design is required to be most efficient and gust-stable UAS on the market.

A summary table of additional information of market competition parameters can be seen in Table 13.

Table 14. Table of market competitors

| Name | MTOW | Payload | Endurance | Range | Speed |
|---|---|---|---|---|---|
| eBee | 1.52 lb | N/A | 50 min | 4.67 mi | 11-25 m/s |
| Lynx M | 8.00 lb | 0.7 lb | 3 hr | 100 mi | 16 m/s |
| Talon 120 LE | 16.0 lb | 2.5 lb | 2.5 hr | 20 mi | 3.6 m/s |
| Penguin B | 47.3 lb | 22 lb | 20+ hr | 930 mi | 22 m/s |
| ITU | 17.0 lb | 2.9 lb | 3 hr | 12.4 mi | 20 m/s |

Therefore, the majority of designs available on the market are either unable to carry sufficient payload, are cost prohibitive to a general consumer, or are not designed to meet the stated end user objectives of this planform. As such, the current market has a dearth of designs that a small-to-midsize company can afford. Additionally, the constraint that the plane is hand-launched is not met by the planes with useful payloads of 5 lb or more. The useful payload modules that the UAV utilizes can be designed by considering the main needs of potential markets and end users of the design.

## A.2 Potential Design Modules

Due to geographic location of the firm, the primary industries of concern are petrochemical, surveying, and agriculture. It is assumed that agriculture surveying

and land surveying have similar design requirements; however, the petrochemical industry presents design challenges that are not faced in solely land-based designs. In addition to offshore delivery UAS, downstream refining plants require extensive air-quality sampling. Therefore, modules should be designed to fit this market. An additional market that can be explored is inter- and intra-city delivery. Modules that allow for each of these markets are used in the engineering design process. A market survey (n=25) was conducted with the following most common results enumerated in Table 15.

Table 15. Common market survey results for modules

| Module | No. Responses |
|---|---|
| Imaging | 22 |
| Delivery | 18 |
| Surveying / 3D map | 13 |
| Air Sampling | 6 |

## A.3 Manufacturing Cost Estimate

A simplified table of part costs is given in Table 16.

Table 16. Major subsystem cost summary

| Assy. No. | Description | Cost |
|---|---|---|
| 01-000 | Wing Frame Subsystem | $125 |
| 02-000 | Wing and Fuselage Skin | $650 |
| 03-000 | Fuselage Frame | $80 |
| 04-000 | Powerplant | $300 |
| 05-000 | Electronics and Controls | $550 |
| 06-000 | Misc. Connectors | $80 |

The total cost for the UAV should be approximately $1800. The major components of the cost are the carbon fiber skin for the fuselage and wings, and the

flight electronics. The customer requirement to have a composite skin requires that such a cost be maintained, and the electronics are required for a SAS to be implemented. Assuming a basic ¼ price model used frequently in industry, the plane must be assembled within 11 hours (at $65/hr). This is sufficient time for wet layup of the wing and fuselage skin, as well as component assembly.

# Appendix B. FAA FAR Part §23 Design

The load factors in design are adherent to 14 CFR Part §23.301-341. A load factor is comparable to g-force experienced by the structure of the plane. A simple free body diagram of a maneuvering load can be seen in Figure 3. Each load factor (n) is defined as a limit load, or a load that must be maintained in perpetuity. The required ultimate loading (1.5n) is not considered in this analysis, as it is simply a design factor of safety.

## B.1 Maneuvering Loading

The primary maneuvering load factor is enumerated in §23.337(a)(1)

$$n = 2.1 + \frac{24000}{W + 10000}$$

for a MTOW of 10 lb, the result is 4.5; however, it is stated in §23.337(a)(1) that +3.8 is the highest load factor that need be considered for normal category planes. The negative load limit, corresponding to a local maximum in flight path, is limited to 0.4n. This, for normal category planes is simply -1.52.

## B.2 Gust Loading

Gust loading is required to meet the gust envelope in §23.333, which, for this design is maximum at a 50 fps gust in cruise ($v_c$). The load factor can be calculated as the final lift on the UAV over the initial cruise lift.

$$n_g = \frac{\frac{1}{2}\rho {v_G}^2 S C_L}{\frac{1}{2}\rho {v_C}^2 S C_L}$$

or simply, assuming all other parameters remain constant within the gust

$$n_g = \frac{{v_G}^2}{{v_C}^2}$$

for the gust speed of 50 fps at a minimum drag speed of 52 fps, this corresponds to a +3.85 load factor.

## B.3 Landing Loading

The landing loading on the design is actually set by the FAA in the testing section of 14 CFR Part 23.

$$h = \frac{3.6}{2}\left({}^{W}/_{S}\right)$$

where h is in inches, and is required to be at least 9.2 inches – used in this design. Using an energy calculation, the energy required to be absorbed by the frame is equal to the potential energy of the height

$$\Delta U = Wh$$

where h is in feet. For a MTOW of 10 lb, this corresponds to 7.67 ft-lb. Using an impulse-momentum approach to force estimation with the time estimated as ${}^{1}/_{10v}$ where v is determined from potential energy, neglecting air resistance. The equations combine to $\bar{F} = \frac{10W}{g}v^2$, or 21.8 lb. Reference [19] suggests using a load factor of 2.6. This will be used in analysis as a conservative load factor.

# Appendix C. Dynamic Thrust Estimation

## C.1 Theory

The theory used to determine the propeller normal and thrust forces is propeller blade theory. This theory uses force and velocity diagrams to transfer known engine output parameters such as brake horsepower (BHP), or torque limits, to the total propeller thrust and normal force [6]. A section view of a typical propeller force diagram can be seen in Figure 49.

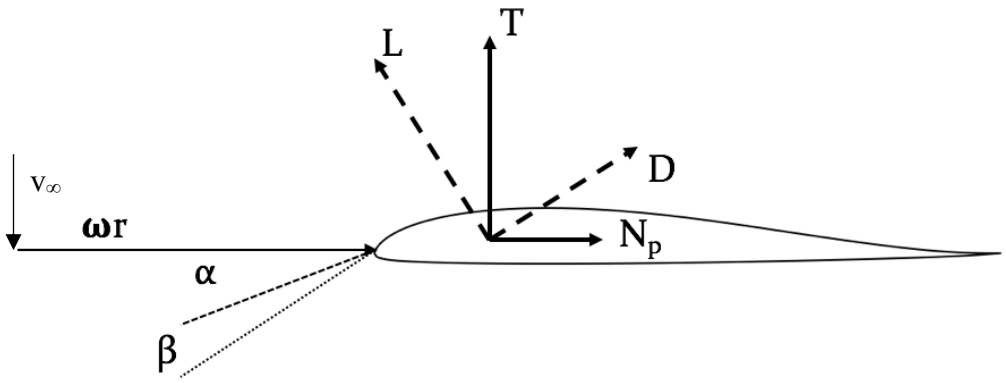


Figure 49. Section view of a typical propeller airfoil with force and velocity diagrams

The force diagram shown in Figure 49 is simply the resolution of the lift and drag forces from the velocity diagram. The velocities that contribute to the force resolution are primarily the rotational velocity (ωr), and the flight speed ($v_\infty$). In a method similar to that outlined in Equations 2.1 – 2.2, the angles between the velocities determined from lift and drag coefficients, and resolved. A more detailed explanation of the theory can be found in Chapter 2 of Reference [6].

## C.2 Code Validation

A validation case for an APC 7x4 SF propeller is used to determine the accuracy of the propeller blade theory code.

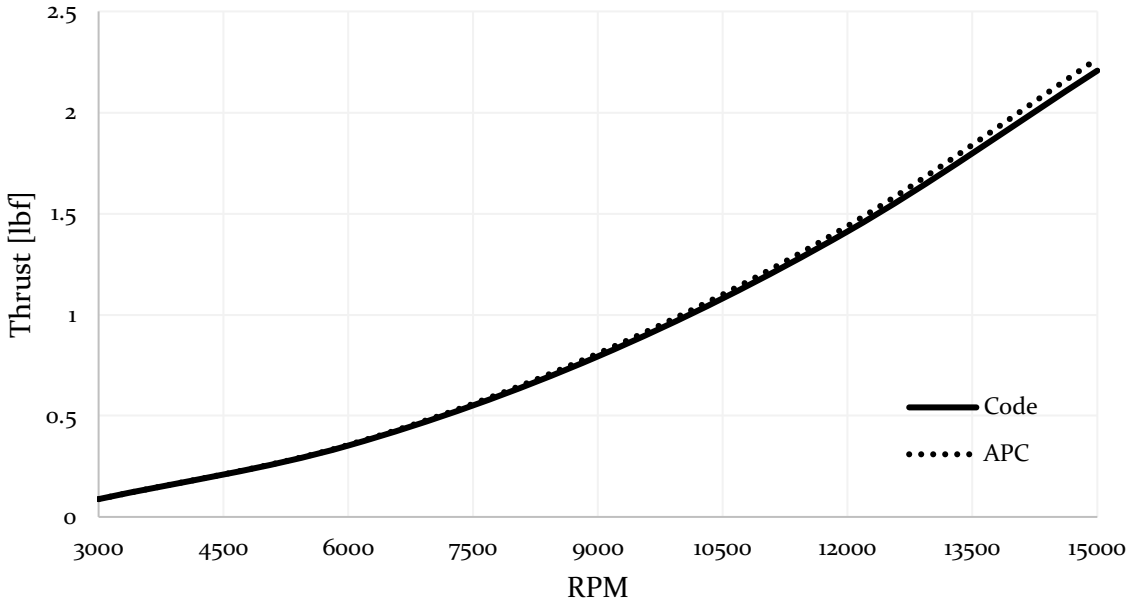


Figure 50. Static thrust estimation curves

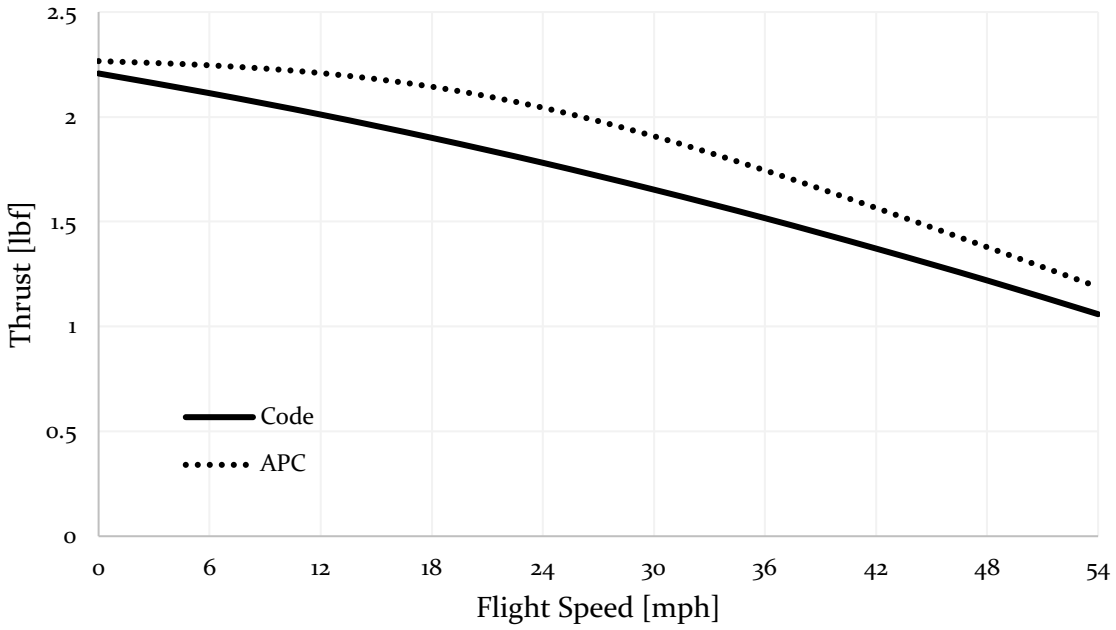


Figure 51. Dynamic thrust estimation curves

The maximum difference between the in-house code and the APC data is 3% in static thrust and 13.5% in dynamic thrust. Differences in the propeller blade code and the APC data likely arise from the assumptions made about the propeller blade shape and airfoil. The code uses a modified linear Clark Y airfoil with the zero-lift angle shifted one degree, as suggested by APC [22]. However, this difference is beneficial in a pusher configuration, as the maximum efficiency loss between a clean propeller (one at the fuselage leading edge) and a pusher propeller is 15%. Therefore, this dynamic thrust code tends to give more realistic pusher data.

## C.3 Results

The results for thrust and normal force were estimated for a tractor (or puller) type propeller. Representative curves for wide open throttle (WOT)

conditions at flight speeds from static (0 ft/s) to the maximum legal flight speed of 100 mph can be seen in Figures 52 and 53 for thrust and normal force, respectively.

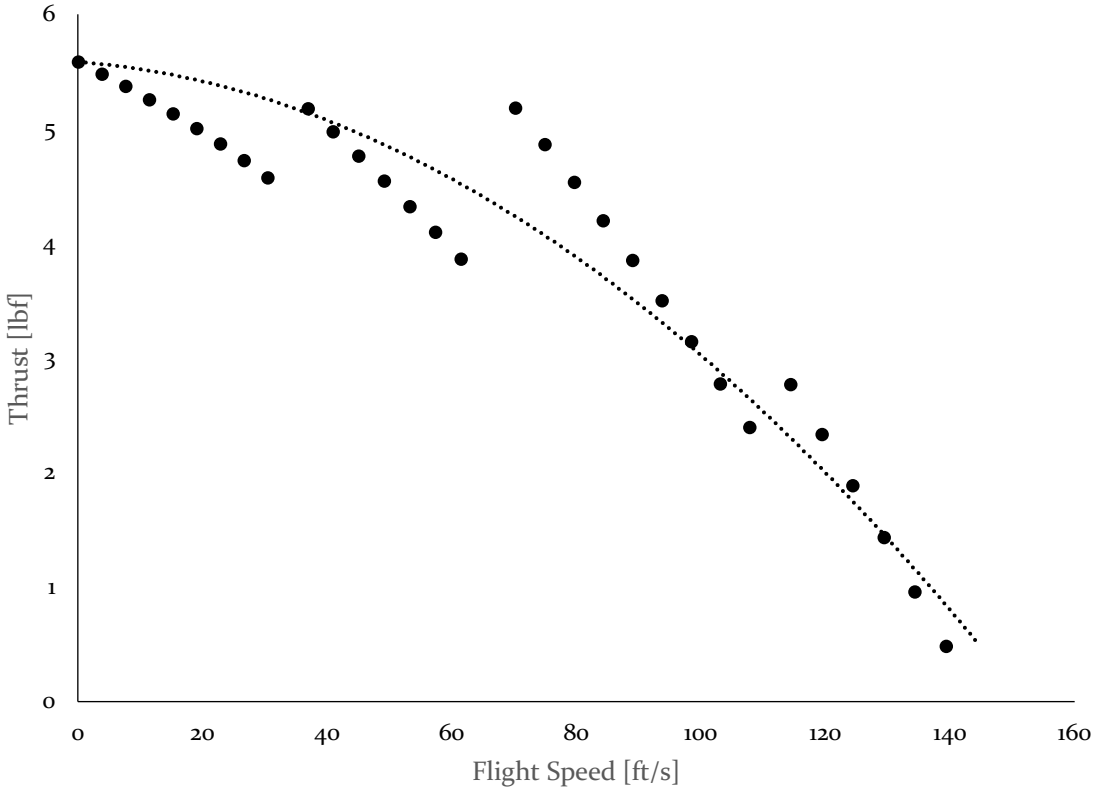


Figure 52. 10x6-4 Propeller thrust force estimate and comparison to APC data

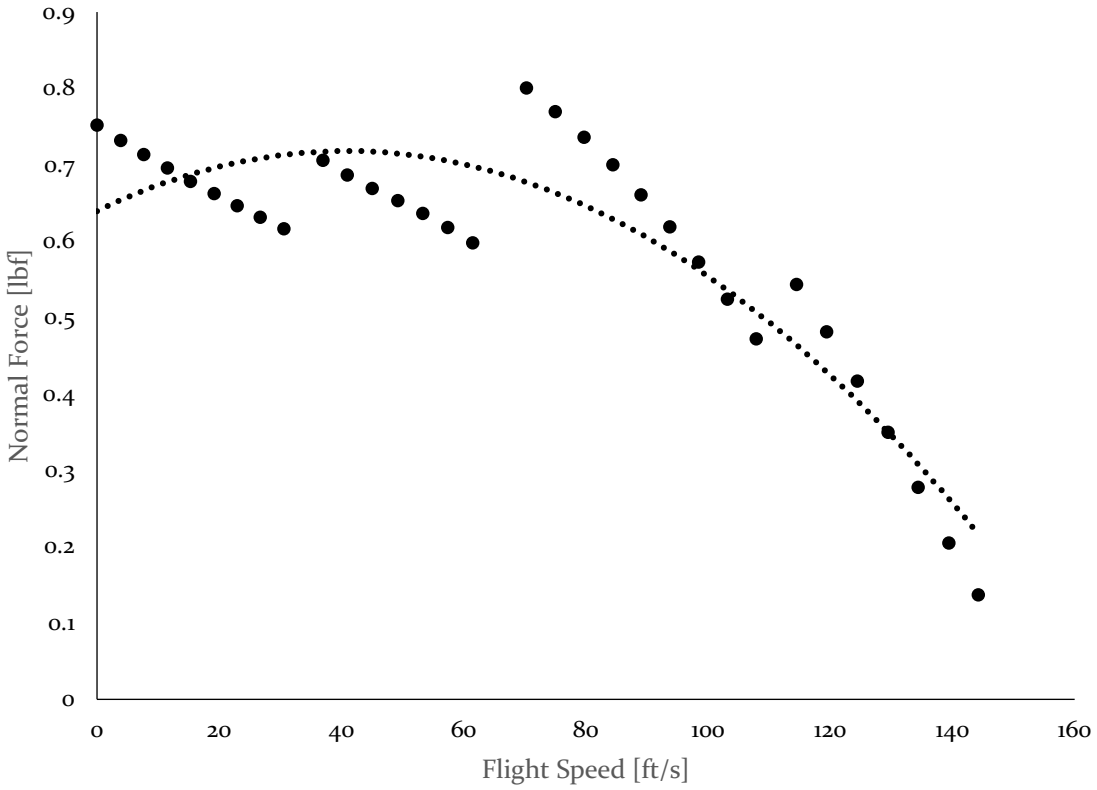


Figure 53. 10x6-4 propeller normal force estimate and comparison to APC data

The results from the code are for smooth transitions between the flight speeds. This data, however, is not available from APC. Therefore, data points were determined by the torque limit from Reference [21]. The thrust force has an $R^2$ value of 0.92, and the normal force has an $R^2$ value of 0.83, corresponding to reasonable values for pre-flight force estimation. The differences in the $R^2$ values of these flight force estimates is due to normal force being a function of torque, while thrust is mostly a function of RPM and flight speed.

# Vita

Sean King graduated from Baton Rouge Magnet High School in 2010. As an undergraduate student at Louisiana State University, he led the Society of Peer Mentors from 2012 to 2014, and led the design projects for incoming engineering majors in 2013 and 2014. Sean has also researched micro-fluidics and been cited on two papers accepted to the IMECE conference in 2011 and 2012.

As a graduate student, Sean has been the teaching assistant for the Mechanical Engineering Department capstone design program. Through this, he has participated in two engineering education conferences, and was the primary author on two papers accepted to ASEE and the Mudd Design Workshop. He has also worked with over 100 client-driven projects with over 500 students during this time.